Isotopic and geochemical constraints on lead and fluid sources of the Pb-Zn-Ag mineralization in the polymetallic Tighza-Jbel Aouam district (central Morocco), and relationships with the geodynamic context

Magali Rossi, Dominique Gasquet, Alain Cheilletz, Leïla Tarrieu, Hassan Bounajma, Tristan Mantoy, Laurie Reisberg, Etienne Deloule, Philippe Boulvais, Pete Burnard

Accepted Manuscript

Isotopic and geochemical constraints on lead and fluid sources of the Pb-Zn-Ag mineralization in the polymetallic Tighza-Jbel Aouam district (central Morocco), and relationships with the geodynamic context

Magali Rossi, Dominique Gasquet, Alain Cheilletz, Leïla Tarrieu, Hassan Bounajma, Tristan Mantoy, Laurie Reisberg, Etienne Deloule, Philippe Boulvais, Pete Burnard

PII: S1464-343X(16)30272-2

DOI: 10.1016/j.jafrearsci.2016.08.011

Reference: AES 2648

To appear in: *Journal of African Earth Sciences*

Received Date: 24 February 2016

Revised Date: 25 July 2016

Accepted Date: 5 August 2016

Please cite this article as: Rossi, M., Gasquet, D., Cheilletz, A., Tarrieu, L., Bounajma, H., Mantoy, T., Reisberg, L., Deloule, E., Boulvais, P., Burnard, P., Isotopic and geochemical constraints on lead and fluid sources of the Pb-Zn-Ag mineralization in the polymetallic Tighza-Jbel Aouam district (central Morocco), and relationships with the geodynamic context, *Journal of African Earth Sciences* (2016), doi: 10.1016/j.jafrearsci.2016.08.011.

Isotopic and geochemical constraints on lead and fluid sources of the Pb-Zn-Ag mineralization in the polymetallic Tighza-Jbel Aouam district (Central Morocco), and relationships with the geodynamic context

Magali Rossi[1*], Dominique Gasquet[1], Alain Cheilletz[2], Leïla Tarrieu[1], Hassan Bounajma[3], Tristan Mantoy[3], Laurie Reisberg[4], Etienne Deloule[4], Philippe Boulvais[5], Pete Burnard[4†]

[1]*Laboratoire EDYTEM, Université de Savoie-Mont Blanc, CNRS-UMR5204, Campus scientifique, 73376 Le Bourget du Lac, France*

[2]*Ecole Nationale Supérieure de Géologie, Laboratoire Géoressources, CNRS-UMR 7359, Université de Lorraine, rue du Doyen Marcel Roubault, BP 40 - 54501 Vandœuvre-lès-Nancy, France*

[3]*Compagnie Minière de Touissit (CMT), 5 rue Ibnou Tofail, Quartier Palmiers, 20340 Casablanca, Centre minier de Tighza, BP 114, M'rirt 54450, Province de Khénifra, Morocco*

[4]*Centre de Recherches Pétrographiques et Géochimiques, CNRS-UMR 7358, Université de Lorraine, BP 20, 54501, Vandœuvre-lès-Nancy, France*

[5]*Géosciences Rennes, Université Rennes 1, CNRS-UMR 6118, 35042 Rennes cedex, France*

*Corresponding author:
Magali Rossi, magali.rossi@univ-smb.fr

Abstract

The W-Au, Pb-Zn-Ag, and Sb-Ba mineralizations of the polymetallic Tighza-Jbel Aouam district (central Meseta, Morocco,), are hosted in Paleozoic rocks surrounding late-Carboniferous granitic stocks. The Pb-Zn-Ag Tighza deposit formed at 254 ± 16 Ma, and is clearly disconnected from the late-Variscan W-Au deposit (295-280 Ma). The Pb-Zn-Ag mineralization precipitated from a complex hydrothermal fluid. It displays air-normalized $^{3}He/^{4}He$ ratio (0.018-0.103) typical of the upper crust. This crustal component is confirmed by the oxygen and carbon isotope compositions ($\delta^{18}O$ = +19 to +25 ‰; $\delta^{13}C$ = -3.6 to -11.2 ‰) and the ε_{Nd} values (-4.84 to -9.01) of gangue carbonates, which show mixing of (i) fluids that have interacted with late-Carboniferous magmatic rocks, and (ii) fluids in equilibrium with the Paleozoic metasediments. In addition, the Pb-Zn-Ag mineralization has $^{40}Ar/^{36}Ar$ values in the range 284-315 typical of a meteoric fluid. The radiogenic Pb isotopic compositions ($^{207}Pb/^{204}Pb$ = 15.70-15.80 and $^{206}Pb/^{204}Pb$ = 18.30-18.50) suggest leaching of Pb from the surrounding Paleozoic metasediments and late-Variscan granites, whereas the low radiogenic signatures ($^{207}Pb/^{204}Pb$ = 15.40 and $^{206}Pb/^{204}Pb$ = 18.05) provide evidence of a deeper source attributed to the lower crust.

Crustal thinning related to extensional tectonics in late-Permian and Early-Triassic lead to high-K calc-alkaline to alkaline magmatic activity, which is evidenced by a dense SW-NE-trending dike network that pre-dated the Atlantic Ocean opening (early Liassic times). This magmatic event induced a regional heat flux increase that triggered the circulation of a complex hydrothermal fluid, which has a strong crustal component, but also a meteoric and a lower crustal components. The polymetallic district of Tighza-Jbel Aouam thus results from superposition of an intrusion related porphyry-gold mineralization (W-Au, 286 Ma) followed by a Pb-Zn-Ag epithermal mineralization (254 Ma), during two distinct magmatic-hydrothermal events.

The proposed metallogenic model for the Pb-Zn-Ag Tighza-Jbel Aouam deposit provides new constraints for the Pb-Zn-Ag exploration in the Moroccan Meseta. Exploration targets must take into account the following geological features: (i) Permo-triassic high-K calk-alkaline to alkaline dikes, (ii) extensional tectonics and reactivation of ancient crust-scale faults and shear zones, and (iii) Paleozoic series containing organic matter (e.g., black shales) subjected to low grade metamorphism (e.g., greenschist facies).

Keywords : Pb-Zn-Ag deposit, Permian-Triassic extensional tectonics, Tighza-Jbel Aouam district, Central Morocco, lead and fluid sources, isotopic (O-C, Sm-Nd, Ar-He, Pb-Pb) data

1. Introduction

West European and Moroccan Paleozoic formations hold numerous volcanogenic massive sulphide (VMS), Mississippi Valley type (MVT), sedimentary exhalative (SEDEX) as well as vein-types Pb-Zn-Ag deposits (e.g., Arribas and Tosdal, 1994; Guilbert and Park, 1999; Marignac and Cuney, 1999; Bouabdellah et al., 2009; Subías et al., 2015, and references therein). Dating of the mineralizing events as well as characterization of the fluid and metal sources are usually difficult to obtain because of fluid mixing, secondary remobilization, and the absence of suitable minerals for dating. As vein deposits frequently occur in close association with late Variscan granites they have long been considered being genetically related to them.

The polymetallic Tighza-Jbel Aouam district (TJAD; central Meseta, Morocco) displays two main types of mineralization, W-Au and Pb-Zn-Ag, hosted in Paleozoic rocks surrounding late-Carboniferous high-K calc-alkaline granitic stocks (Agard et al., 1958; Cheilletz, 1984; Jébrak, 1984; Nerci, 2006; Marcoux et al., 2015; Rossi et al., 2016). It has long been considered to have a single magmatic-hydrothermal origin due to the spatial zoning of mineralization around a supposed hidden batholith (Agard et al., 1958; Desteucq, 1974). The W-Au mineralization and related potassic alteration from the “Mine Granite” are coeval and dated at 286 ± 0.4 Ma (Cheilletz et Zimmermann, 1982; Nerci, 2006; Watanabe, 2002). Based on field observations and isotopic studies, Agard et al. (1958), Cheilletz (1984), Jébrak (1984) and Marcoux et al. (2015) suggested that the Pb-Zn-Ag ore was emplaced after the W-Au deposit without further precision on the time gap. However, Marcoux et

al. (2015) consider the Pb-Zn-Ag mineralization to be the last stage of a reduced intrusion-related gold deposit, with fluid focusing at the top of the solidified and cold intrusion. The hydrothermal activity associated with the Pb-Zn-Ag deposit was recently dated at 254 ± 16 Ma (Tarrieu, 2014; Cheilletz et al., 2015; Rossi et al., 2016), demonstrating the disconnection between the Pb-Zn-Ag mineralization and the W-Au mineralization. A new metallogenic model, based on the disconnection from spatially associated granites, needs to be considered for the TJAD. This model could be applied to other Pb-Zn-Ag deposits in similar geological context.

The source of the W-Au mineralization is strongly constrained by field geology, geochemical changes related to K-alteration, fluid inclusions analysis and Pb-Pb isotopes (Cheilletz, 1984; Nerci, 2006; Marcoux et al., 2015). However, only scarce fluid inclusion, Sr-Nd and Pb-Pb isotopic data are available for the Pb-Zn-Ag deposit (Nerci, 2006; Castorina and Masi, 2008; Marcoux et al., 2015). This paper aims to to better constrain the fluid and the lead sources of the Pb-Zn-Ag mineralization, by combining rare earth elements (REE) data and C-O, Sm-Nd, Ar-He and Pb-Pb, isotopes. The isotopic signatures of gangue carbonates and galena are used as tracers of the crustal, mantellic and meteoric reservoirs. The mineralizing events are finally integrated into the late-Variscan to Permo-Triassic geodynamic framework, in order to propose an updated metallogenic model and new exploration guides.

2. Geological setting and deposit geology

2.1. Geology of Central Morocco

The Tighza-Jbel Aouam district (TJAD) belongs to the central Meseta of Morocco, which is composed of an early to middle Paleozoic basement intruded by late Carboniferous granites (Gasquet et al., 1996; Michard et al., 2008) as well as by numerous Permo-Triassic intermediate to felsic dikes (Gasquet and Bouloton, 1995) and Permian volcanic rocks (Youbi et al., 1995; Figure 1). The Paleozoic rocks are covered by Mesozoic-Cenozoic sedimentary formations. The felsic intrusive rocks are spatially associated with W, Sn, F, Sb and Pb-Zn-Ag deposits (Agard et al., 1958; Cheilletz, 1984; Jébrak, 1984; Boutaleb, 1988; Giulani et al., 1989; Boushaba and Marignac, 2009). The Meseta domain corresponds to a complex collage of terranes representing several Variscan tectonic phases since Devonian times (Figure 1; Michard et al., 2008; Murphy et al., 2016). The main Variscan collisional events resulted in crustal thickening, folding and Variscan granite emplacement. The latest collisional phase involved NW-verging fold, duplexes and nappes (Michard et al., 2008, and references therein). Late-Carboniferous and Permian transtensive events followed, as evidenced by intra-continental basins that have been moderately deformed before the Atlasic cycle. These basins are opened by reactivation of old Variscan faults due to crustal thinning (El Hadi, 2006). The Permian sedimentary sequence is characterized by detrital sedimentation (conglomerates, sandstones and argillites) with interbedded volcanic rocks and associated dikes that crosscut the sedimentary pile (Piqué et al., 2011). Finally, the extensive tectonic regime develops during Triassic, with the opening

of large sedimentary basins that preceded the Atlantic Ocean opening and related CAMP activity (Mahmoudi and Bertrand, 2007; Vérati et al., 2007).

2.2. Geology of the Tighza-Jbel Aouam district (TJAD)

The TJAD has long been known for its W-Au mineralization, as well as for major Pb-Ag-Zn and minor Sb-Ba mineralizations, hosted in Paleozoic metasediments (Agard et al., 1958; Desteucq, 1974; Cheilletz, 1984; Jébrak, 1984; Wadjinny, 1998; Nerci, 2006; Tarrieu, 2014; Marcoux et al., 2015). Upper Visean (Mississippian) limestones and schists unconformably overlie Ordovician siliceous schists and quartzites, Silurian black shales, and Devonian siliceous limestones. These Paleozoic metasediments are deformed into a succession of SW-NE-trending anticlines and synclines, and are metamorphosed up to greenschist facies. The TJAD is localized between two crustal-scale E-W shear zones that controlled the opening of tension veins and dikes during late and post-Variscan time (Figures 1 and 2).

The Paleozoic formations are crosscut by microgranite and micogranodiorite dikes, and by four monzogranite stocks named, from South to North, Kaolin, Mine, Mispickel, and Tighza peaks. The high-K calc-alkaline signature of all of these intrusive bodies is observed in most Moroccan Variscan granites and reflects either an enriched mantle or a lower crustal component (Gasquet et al., 1996; El Hadi et al., 2006). The monzogranite stocks have been dated at 320-300 Ma by Tarrieu (2014) and Rossi et al. (2016).The three southernmost stocks are surrounded by a large and well-delimited biotitic alteration halo related to the W-Au mineralizing event (Figure 2; Cheilletz, 1984; Cheilletz and Isnard, 1985). The gravimetric study of El Dursi (2009), carried out on the TJAD, suggests that this hydrothermal alteration halo is associated with a hidden thin and shallow intrusive pluton. The W-Au mineralization thus results from a second magmatic stage at 295-280 Ma. It can be considered as a porphyry-type deposit based on (i) the genetic link with calc-alkaline magmatic activity (Cheilletz, 1984; Marcoux et al., 2015), (ii) potassic alteration related to a hidden pluton (Cheilletz and Zimmermann, 1982; Cheilletz, 1984), (iii) high temperature hydrothermal fluids that have a magmatic signature (Nerci, 2006; Marcoux et al., 2015), and (iv) the occurrence of disseminations, W-rich skarns, stockworks, sheeted veins and large veins. The large E-W-trending veins formed during a dextral transpressive regime (Cheilletz, 1984).

The currently mined Pb-Zn-Ag mineralization, which crosscuts the W-Au ore (Figure 3), has been dated at 254 ± 16 Ma (Tarrieu, 2014; Cheilletz et al., 2015; Rossi et al., 2016). It developed during a magmatic-hydrothermal episode associated with emplacement of a dense network of late-Permian dikes, found throughout the Moroccan Meseta (Bouloton and Gasquet, 1995; Gasquet and Bouloton, 1995; Rossi et al., 2016). The Pb-Zn-Ag mineralization is filling NE-SW transtensive tension-gashes that developed during a NW-SE compression. The old dextral E-W shear zones are reactivated with a sinistral component during this tectonic event. Fluid inclusions analyses and calculated isochores

allowed Nerci (2006) and Marcoux et al. (2015) to constrain minimum trapping P-T conditions (see 2.3.).

The polymetallic TJAD thus results from two successive magmatic-hydrothermal events that produced first the W-Au mineralization followed by the Pb-Zn-Ag mineralization (Tarrieu, 2014; Rossi et al., 2016).

2.3. Geology of the Pb-Zn-Ag mineralization

The Pb-Zn-Ag mineralization has been mined since 1930 from several large extensional veins with N25°E to N75°E orientations (Figure 2). In most cases, the veins display a "Y" shape, showing a connection between two veins, which suggest fracture opening as part of a conjugate strike-slip fault system (see Cheilletz 1984 for details; Figure 2). The main Pb-Zn-Ag veins are, from North to South: Filons Parallèles and Filon Nord, Filon Signal and Structure 18, Structure II, Sidi Ahmed, Ighrem Aousser and Iguer Oujna. Only Filon Signal, Structure 18, Sidi Ahmed and Ighrem Aousser are currently being mined, allowing extensive observations and sampling of fresh rocks.

The Pb-Zn-Ag mineralization comprises sulphides (galena + sphalerite) in a gangue of carbonates (calcite ± siderite and ankerite) ± quartz (or red chalcedony). Development of the deposit was associated with weak carbonate alteration of the Paleozoic country rocks. Analyses of fluid inclusions trapped in calcite from Sidi Ahmed vein indicate that the Pb-Zn-Ag mineralization formed at a minimum temperature of 230°C, from Na-Ca brines and a complex fluid with organic compound. Calculated isochores indicate hydrostatic pressures of at least 30 MPa (Nerci, 2006; Marcoux et al., 2015).

The paragenetic sequences are slightly different among the different veins. In Filon Signal and Structure 18, the mineralization is typically banded and rather symmetrical: vein minerals grew from the edge of the vein towards its center (Figure 4). These large veins display a succession of four paragenetic assemblages (Figure 4 and Figure 5): (P1) quartz + siderite, (P2) galena + calcite ± sphalerite, (P3) galena + sphalerite + siderite, and (P4) calcite + quartz + pyrite. As shown in Figure 4, the early barren P1 assemblage is not present everywhere. The Pb-Zn-Ag mineralization is associated with P2 and P3 assemblages (Figure 4 and 5). The latest hydrothermal phase (P4) is barren.

In Sidi Ahmed and Ighrem Aousser, the four hydrothermal successive events (pulses) display slightly different paragenetic assemblages than in Filon Signal and Structure 18 (Tarrieu, 2014; Rossi et al., 2016, Figure 5): (P1) hydraulic fracturing and precipitation of siderite + quartz, (P2) banded galena + ankerite ± sphalerite, (P3) brecciation and precipitation of galena + sphalerite, and (P4) calcite + quartz + pyrite. Jébrak (1984, 1985) noted that gangue carbonates are REE-rich.

3. Sampling and analytical methods

In order to provide insights into the lead and mineralizing fluid sources of the Pb-Zn-Ag mineralization, various complementary isotopic studies have been performed on sulphide minerals

(He-Ar on pyrite and sphalerite, Pb isotopes on galena) and on gangue siderite, ankerite and calcite (O-C isotopes, Sm-Nd, REE content). Most samples were collected within the three main Pb-Zn-Ag veins, Filon Signal, Sidi Ahmed and Ighrem Aousser veins. They were collected underground in order to provide unweathered rocks. Some additional samples were also collected from drill cores from Filon Nord and Filons Parallèles, i.e., from the northernmost veins (Figure 2).

3.1. REE content of carbonates

Four siderite (P1), six ankerite (P2) and thirteen calcite (P4) concentrates sampled in the various Pb-Zn-Ag veins were analyzed by ICP-MS at the SARM-CRPG in Nancy, France. The minerals were concentrated by handpicking. The analytical results are presented in Table 1 and Figures 6 and 7.

3.2. Stable isotopes (O, C)

Carbon and oxygen isotope analyses were carried out at the stable isotope laboratory of Géosciences Rennes (France). Analyses were performed on separated siderite, ankerite and calcite crystals sampled in Signal, Sidi Ahmed and Ighrem Aousser veins. Carbonate materials were reacted with anhydrous H_3PO_4 at 50°C during fifteen hours. Isotopic measurements on the liberated CO_2 were made using a VG SIRA-10 triple collector mass spectrometer. Isotopic compositions are quoted using the δ notation with respect to SMOW for $\delta^{18}O$ and PDB for $\delta^{13}C$. Measured carbonate $\delta^{18}O$ - $\delta^{13}C$ values have been corrected using the NBS19 international and Prolabo Rennes in-house standards values. Analytical precisions are estimated to be ±0.1‰ and ±0.15‰ respectively for the $\delta^{13}C$ and $\delta^{18}O$ in carbonates. Results are presented in Table 2 and Figure 9.

3.3. Sm-Nd

In order to complete the data obtained by Castorina and Masi (2008) on siderites from Signal and Sidi Ahmed, Sm and Nd isotope analyses were performed in CRPG Nancy on ankerite and calcite from from Sidi Ahmed and Ighrem Aousser. After addition of a mixed ^{150}Nd-^{147}Sm spike, samples were digested in HF + HNO_3, and Sm and Nd were extracted by chromatographic techniques adapted after those of Pin et al. (1997) using TRU spec and LN spec resins. Sm and Nd isotopic compositions were determined by MC-ICP-MS (Neptune). During the period of analysis the JNdi-1 Nd standard yielded 0.512095 ±0.000014 (2σ, 11 analyses) Analytical blanks represented <1% of the total amount of Nd analyzed in all cases and are thus negligible. Results are reported in Table 3 and Figure 10.

3.4. Rare gases Ar-He

Sulphides from the W-Au (2 As-pyrite and 1 pyrite) and Pb-Zn-Ag mineralization (2 pyrites and 1 sphalerite from Sidi Ahmed) were carefully selected under a binocular microscope to eliminate alteration and inclusions, and then crushed. The analyses were performed by P. Burnard at the CRPG –CNRS (Nancy, France) following the analytical procedure of Marty and Zimmermann (1999). The

amounts and the isotopic ratios of helium and argon were analyzed with a VG 5400 rare gas mass spectrometer. Results are reported in Table 4 and Figure 11.

3.5. Lead isotopes

Six ore samples were selected from the three main veins for in-situ Pb isotope analysis on galena (n_{gn}) and sphalerite (n_{sph}) individual grains. 32 galena and 32 sphalerite crystals were analysed from Signal vein: n_{gn} = 3 and n_{sph} = 12 in Tz10/39; n_{gn} = 25 and n_{sph} = 10 in Tz11/42; n_{gn} = 4 and n_{sph} = 20 in Tz10/43). 7 galena crystals were analysed in sample Tz10/35 from Sidi Ahmed vein. 8 galena and 11 sphalerite crystals were analysed from Ighrem Aousser vein: n_{gn} = 5 in Tz10/30; n_{gn} = 3 and n_{sph} = 112 in Tz10/31. Measurements were performed in CRPG-CNRS (Nancy, France) by ion microprobe following Deloule et al. (1986), using the Cameca IMS 3F for Tz10/30 at a mass resolution of 800, and the Cameca IMS 1270 in monocollection mode to a mass resolution of 4000 for the other samples. All data are reported in Table 5 and Figure 12.

4. Results and interpretation

4.1. REE content of carbonates

The total REE content of siderite, ankérite and calcite from the Tighza Pb-Zn-Ag veins ranges between 45 and 4041 ppm (n=44, Figure 6 and Table 1; Jébrak, 1985; Castorina and Masi, 2008; this study). About 50% of the analysed carbonates have rather low total REE content (< 300 ppm), but 14 samples are significantly REE-rich and contain more than 900 ppm REE (up to 4000 ppm). Such content is unrelated to the mineralogy or to the paragenetic stages considering that the most enriched carbonates are a P2-ankerite (4041 ppm) and a P4-calcite (2702 ppm) in Ighrem Aousser, a P3-siderite crystal in Sidi Ahmed (2385 ppm; Castorina and Masi, 2008), and a P2-ankerite crystal in Signal vein (2400 to 2700 ppm; Jébrak, 1985). Changes in REE content might reflect changes in growth or fluid flow rates (Möller et al., 1991) or changes in temperature (Möller et al., 2004). As P4-calcite crystals cover a large REE range within a single vein, this scatter is unlikely due to variation of the fluid temperature but rather to changes in fluid-flow rates, thus on fluid-rock ratios, depending on variable degrees of vein opening.

PAAS-normalized REE+Y patterns of gangue carbonates allow identification of two distinct groups. Most carbonates from the Signal, Sidi Ahmed and Ighrem Aousser lodes have similar PAAS-normalized REE+Y patterns (Group 1), characterized by $(La/Sm)_N$ lower than 1 (0.06 to 0.60), $(Gd/Lu)_N$ higher than 1 (1.25 to 13.52), and positive Eu_N anomalies (1.5 to 3.0; Figure 7, Table 1). Whatever the vein, the carbonate (siderite, ankerite or calcite) or the paragenetic sequence, all carbonates from group 1 display similar REE+Y patterns, suggesting that they crystallized from a unique hydrothermal fluid. The various paragenetic sequences reflect the evolution of the reactive fluid composition due to fluid-rock interaction. Regardless of mineralogy and paragenetic sequences, half of group 1 carbonates have $(La/Lu)_N$ lower than 1 (0.1 to 1.0), and half have $(La/Lu)_N$ higher than

1 (1.0 to 5.6). Different pH conditions (Castorina and Masi, 2008) or changes in temperature could explain these differences. The upward-convex shape REE+Y patterns are typical of hydrothermal fluids and carbonates that precipitated from hydrothermal crustal fluids in various geological contexts (e.g., Michard, 1989; Lüders et al., 1993; Hecht et al., 1999; Torres-Ruiz 2006, Margoum et al., 2015, and references therein). Therefore, the REE+Y patterns of gangue carbonates are representative of the hydrothermal fluid, so that it not possible to discriminate among the possible crustal sources of REE (local sedimentary and magmatic host-rocks, or other crustal sources) based on REE+Y patterns only. As already discussed by Castorina and Masi (2008), the slight negative Ce_N anomaly, which is typical of marine carbonate, likely reflect fluid-carbonate interaction or a slight contribution of seawater. The positive Eu_N anomalies could either reflect (i) REE mobilization at high-temperature, and precipitation at lower temperature (> 200-250°C) under reducing and mildly acidic conditions (Bau 1991; Bau and Möller, 1992), (ii) inheritance from host-rock alteration, or (iii) chemical complexation reactions or sorption effects. As fluid inclusions indicate that the Pb-Zn-Ag mineralization precipitated at a minimum temperature of 230°C (Nerci, 2006; Marcoux et al., 2015), the observed positive Eu_N anomalies most likely result from temperature conditions of REE mobilization and precipitation (Bau 1991; Bau and Möller, 1992). Finally, the hydrothermal fluid probably has interacted with upper crustal rocks and marine carbonates, under rather high temperatures in order to mobilize REE+Y, and then precipitated at temperature higher than 230°C.

Two P4-calcite crystals sampled in late-calcite veins show different PAAS-normalized REE+Y patterns (Group 2), with $(La/Sm)_N$ lower than 1 (0.33 and 0.45), $(Gd/Lu)_N$ lower than 1 (0.32 and 0.61), and negative Eu anomalies (0.46 and 0.59; Figure 11). The HREE enrichment, as well as the strong positive Y_N anomalies are similar to those found in marine carbonates (Hu et al., 1988; Nothdurft et al., 2004), suggesting these two calcites might have precipitated either from a fluid with a rather strong seawater component, or that interacted mostly with marine carbonates.

The high REE content of gangue carbonates results from microscopic solid inclusions of REE-rich minerals evidenced from SEM observation (Figure 8). More than 95% of the analyzed REE-rich crystals are La-rich synchysite (i.e., Ce-Y-Nd-La-bearing fluorocarbonate; Figure 8). Destabilisation reaction of rare xenotime and monazite into synchysite has been observed (Tarrieu, 2014), suggesting that at least some of the synchysite crystals are secondary phases. The mineralogical reaction follows the equation:

(Ce, La, Nd)-monazite + xenotime + calcite + H_2O-CO_2-F-rich fluid =>

(Ce, La, Y, Nd)-synchysite + acidic-PO_4-rich fluid

According to this equation, circulation of a H_2O-CO_2-F-rich fluid is required, and REE+Y remain immobile. The occurrence of these REE-bearing minerals explains most of the total REE content of gangue carbonates. Indeed, Ce accounts for 24 to 40 % of the total REE content of carbonates, Nd for about 20 % and La for 5 to 20 %. Yttrium is also quite abundant and represents 15 to 25 % of total

REE+Y content (Table 1). Such Ce:La:Nd:Y ratios are in the same range than in the synchysite composition.

In the TJAD, the high REE contents of gangue carbonates from the Pb-Zn-Ag mineralization is mainly due to the occurrence of abundant solid inclusions of (Ce, La, Y, Nd)-rich synchysite micro-crystals that precipitated from the hydrothermal fluid.

4.2. Stable isotopes (O, C)

No systematic difference between the stages of carbonation is evidenced from table 2, regardless the nature of the gangue carbonate. Rather, each carbonate mineral tends to display specific carbon isotope composition: siderite crystals range between $\delta^{13}C$ = -5.12 ‰ and -4.15 ‰, ankerite crystals range between -3.6 ‰ and -5.1 ‰, whereas apart from one sample ($\delta^{13}C$ = -2.5 ‰), calcite crystals are more depleted in ^{13}C and range between -11.2 ‰ and -5.7 ‰. With the exception of two calcite crystals ($\delta^{18}O$ = 11.9 ‰ and $\delta^{18}O$ = 16.1 ‰), carbonate grains display similar and homogeneous $\delta^{18}O$ values, in the 19-25 ‰ range.

Figure 9 indicates that gangue carbonates plot in the range of hydrothermal carbonates. Calculation of the isotopic composition of the hydrothermal fluid in equilibrium with gangue carbonates is required in order to determine the origin of the hydrothermal fluid. Based on fluid inclusion analysis performed on galena from Signal vein, Nerci (2006) and Marcoux et al. (2015) estimated a minimum trapping temperature of about 230°C for the Pb-Zn-Ag veins. The oxygen isotope composition of the fluid in equilibrium with gangue carbonates was calculated for the range 230°C-300°C using the temperature-dependent calcite-H_2O fractionation factors of Zheng (1999). The carbon isotope composition of CO_2 was calculated for the same temperature range using the temperature-dependant calcite-CO_2 fractionation factors of Chacko et al. (1991), assuming a similar fractionation for siderite and ankerite. The $\delta^{18}O$ values of the hydrothermal fluid are consistent with those of a fluid in equilibrium with the surrounding shales (Tartèse et al., 2012; Figure 9). The calculated $\delta^{18}O$ compositions of fluids in equilibrium with calcite crystals show significant variability. Indeed, two calcite samples display low oxygen isotope compositions, which likely reflect crystallization at higher temperature, from a low-$\delta^{18}O$ fluid component and/or variable fluid–rock ratios. The carbon isotope compositions of the hydrothermal fluid cover a wide range, between -9.6 ‰ and -2.1 ‰. As calcite-CO_2 carbon fractionation is rather limited at 230-300°C, this large interval is unlikely the result of crystallization at variable temperature. It most likely reflects mixing between two end-members. The enriched ^{13}C end-member could either be attributed to seawater-derived fluid or to a fluid that underwent interaction with ancient marine carbonates. The occurrence of carbonate-rich crustal rocks in Devonian and Visean metasediments (sandy limestone and limestones + calcschists respectively) of the TJAD, and their possible occurrence in some underlying Cambrian and Proterozoic rocks (Gasquet et al., 2008; Pereira et al., 2015; and references therein) is consistent with the latter hypothesis. The depleted ^{13}C end-member has $\delta^{13}C$ values typical of fluids with some organic carbon, regardless of their origin. It

would be hazardous to specify the exact source of fluid on the basis of the $\delta^{13}C$ signature considering that (i) Pb-Zn-Ag mineralization is coeval with magmatic activity, (ii) the surrounding Paleozoic metasediments contain some organic matter, especially the Siluro-ordovician black shales and schists, and (iii) the $^{40}Ar/^{36}Ar$ ratios of sulphide crystals provide evidence of the infiltration of meteoric fluids. Therefore, the carbon and oxygen compositions suggest that gangue carbonates precipitated from a H_2O-CO_2-rich fluid, with a strong crustal component, that equilibrated with the Paleozoic metasedimentary pile hosting the Pb-Zn-Ag mineralization.

4.3. ε_{Nd} results

Calcite and ankerite samples have rather similar Sm/Nd ratios and Nd isotopic compositions to those of siderites from Castorina and Masi (2008; Table 3), with $^{147}Sm/^{144}Nd$ = 0.1381 to 0.2532 and ε_{Nd} = -4.84 to -9.01. ε_{Nd} values were calculated at the age of Pb-Zn-Ag ore formation (about 255 Ma; Rossi et al., 2016). Results are presented in Table 3 and Figure 10. All carbonates display $\varepsilon_{Nd\text{-}255Ma}$ values of -4 to -8. This range lies between the Paleozoic schists and the late-Carboniferous granitic stocks values (Schaltegger et al., 1994; Castorina and Masi, 2008; Marcoux et al., 2015), suggesting Nd could derive from these two crustal reservoirs. Permian rocks overlying the paleozoic schists at the time of the Pb-Zn-Ag hydrothermal event, and deeper crustal rocks could also be taken into consideration. As these rocks are not cropping out in the Central Meseta, there is no geochemical data available, so that their contribution is not being discussed below. The contribution of the two assumed local crustal reservoirs seems to be variable considering that some siderites have ε_{Nd} values similar to those of some granitic stocks from the district, whereas calcites display values close to those of Paleozoic basement rocks.

Castorina and Masi (2008) estimated a contribution of about 50 % for each reservoir, but they considered leaching to have occurred at 280 Ma. Considering that Pb-Zn-Ag ore formed at 255 Ma (Rossi et al., 2016) the basement contribution was estimated for each sample, using the equation below with average $\varepsilon_{Nd\text{-}255Ma}$ values of -2.32 for the granitic stocks and of -10.21 for basement schists (Castorina and Masi, 2008; see Table 3):

$$\% \text{ basement} = (\varepsilon_{Nd\ sample} - \varepsilon_{Nd\ granite})/(\varepsilon_{Nd\ sample} - \varepsilon_{Nd\ granite})$$

Nd from Paleozoic schists would thus contribute 58-71 % in calcite, 44-64 % in ankerite, and 22 to 59 % in siderite (using data from this study and from Castorina and Masi, 2008).

4.4. Rare gases Ar-He

The W-Au and Pb-Zn-Ag mineralizations have rather similar $^{40}Ar/^{36}Ar$ ratios, ranging between 284 and 328 (Figure 11), with the exception of one data point. Such values are similar to meteoric Ar ($^{40}Ar/^{36}Ar$ = 295.5; Steiger and Jäger, 1977), providing evidence of infiltration of a meteoric and/or air-equilibrated fluid for both mineralization. On the contrary, two distinct signatures are evidenced from He isotopes (Figure 11): (i) the W-Au mineralization displays rather high air-normalized $^{3}He/^{4}He$

ratios, ranging from 1.083 to 1.814, whereas (ii) the Pb-Zn-Ag mineralization displays very low air-normalized $^{3}He/^{4}He$ ratios, in the range 0.018-0.103.

Possible artifacts such as cosmogenic production of ^{3}He, nucleogenic production of ^{3}He from reaction with a Li-rich crustal fluid, and isotopic fractionation during He-leakage have been discarded to explain the measured $^{3}He/^{4}He$ ratios because: all samples were collected several hundred meter below the surface or from drillcores, so they cannot be affected by cosmogenic radiation; Li does not substitute for Pb in galena (Kendrick et al., 2005) and fluid inclusion studies provided no evidence of interaction with a Li-rich fluid (Marcoux et al., 2015); and if fractionation occurred during leakage, preferential escape of ^{3}He over ^{4}He from galena would have produced $^{3}He/^{4}He$ ratios lower than crustal values, which has not been observed (Kendrick et al., 2005; Bouabdellah et al., 2015). The measured $^{3}He/^{4}He$ ratios are thus assumed to reflect mixing between atmospheric, crustal and mantle-derived He ($^{3}He/^{4}He_{atmt} = R_a = 1.39x10^{-6}$; $^{3}He/^{4}He_{crust} = 0.01\text{-}0.05\ R_a$; $^{3}He/^{4}He_{mantle} = 6\text{-}9\ R_A$; Andrews, 1985; Porcelli et al., 1992, Burnard et al., 1999; Burnard and Polya, 2004).

Even though a sample has a $^{3}He/^{4}He$ ratio similar to atmospheric He, a contribution of atmospheric He is rather unlikely for the W-Au ores. Considering a $^{3}He/^{4}He_{mantle}$ ratio of 6 R_A, more than 95 % of He from the W-Au ores would derive from atmospheric He, which is very unlikely considering that the W-Au mineralization is genetically related to late-Variscan calk-alkaline magmatic activity (Cheilletz, 1984; Cheilletz and Isnard, 1985; Marcoux et al., 2015). Assuming atmospheric He contribution is negligible for the W-Au mineralization, and considering a $^{3}He/^{4}He_{crust}$ ratio of 0.01 R_A,18 % to 30 % of the ^{4}He derived from the mantle and 70% to 82% derived from the crust.

Sulphides from the Pb-Zn-Ag mineralization have air-normalized $^{3}He/^{4}He$ ratios in the same range as crustal He. ^{4}He thus essentially has a crustal component and only exhibits very limited mixing with atmospheric He (< 5 %) or mantle-derived He (< 2%).

4.5. Lead isotopes

Lead isotope ratios from the Pb-Zn-Ag (galena) and the W-Au (mispickel and löllingite) ores as well as data from the outcropping granitic stocks (K-feldspar) are presented in Figure 12 and Table 5 (Watanabe, 2001; Nerci, 2006; Marcoux et al., 2015; Tarrieu, 2015; Cheilletz et al., 2015). The lead isotope signatures of sphalerite crystals show huge dispersion so that it is impossible to interpret the data; they are thus not taken into consideration. Lead isotope data of galena samples spread between a highly radiogenic end-member ($^{207}Pb/^{204}Pb = 15.70$ to 15.80) and a much less radiogenic one ($^{207}Pb/^{204}Pb = 15.40$), thus suggesting mixing of distinct sources of lead. The dataset is bordered by two mixing lines corresponding to the *ca.* 320 Ma and the *ca.* 255 Ma geochrons (trends A and B respectively in Figure 12) that crosscut the crustal evolution curves of Stacey and Kramers (1975) and Ludwig et al. (1989). Galena samples following trend A plot between lead isotope ratios observed in K-feldspars from the outcropping stocks ($^{207}Pb/^{204}Pb = 15.70$ and $^{206}Pb/^{204}Pb = 18.30$) and a less radiogenic composition ($^{207}Pb/^{204}Pb = 15.55$ and $^{206}Pb/^{204}Pb = 18.15$). Galena samples following trend

B plot between highly radiogenic ($^{207}Pb/^{204}Pb = 15.80$ and $^{206}Pb/^{204}Pb = 18.50$) and much less radiogenic values ($^{207}Pb/^{204}Pb = 15.40$ and $^{206}Pb/^{204}Pb = 18.05$). Trends A and B are not associated with specific veins or samples. Indeed, galena samples from Signal vein (blue symbols), as well as from Sidi Ahmed (green symbols), plot on both trends. Furthermore, some galena crystals from sample Tz10/42 (Signal vein) plot along trend A, some along trend B, and the others plot between the two trends, suggesting remobilisation of lead from different sources.

The least radiogenic ratios observed in the $^{207}Pb/^{204}Pb$ versus $^{206}Pb/^{204}Pb$ diagram suggest a deep source of lead such as the mantle or lower crust (e.g., Zartman and Haines, 1988; Figure 12). In contrast, the most radiogenic ratios clearly indicate leaching of lead from the upper crust. A possible source of radiogenic lead could thus be the outcropping granitic stocks. U-Pb dating of zircons from the magmatic stock indicates a crystallisation age of 320-300 Ma, whereas dating of monazite hosted in gangue carbonate yields an age of 254 ± 16 Ma for the Pb-Zn-Ag ore (Rossi et al., 2016). As leaching of magmatic lead occurred several million years after the stocks crystallization, radiogenic ingrowth of Pb in U-rich magmatic crystals must be considered in order to determine the isotopic composition of the granitic stocks at the time of galena formation. Considering K-feldspar recorded the magmatic isotopic composition at the time of crystallization (*ca.* 320 Ma), the lead isotope signature of the granitic stocks at 255 Ma can be estimated at $^{207}Pb/^{204}Pb = 15.70$ and $^{206}Pb/^{204}Pb = 18.40$, using a $^{238}U/^{204}Pb$ ratio of 9.735 (e.g., Faure and Mensing, 2005). Such ratios fit well with trend B (Figure 12), suggesting leaching at 255 Ma of lead from U-rich magmatic minerals formed at 320-310 Ma in the granitic stocks. As these stocks are rich in magmatic sulphides that contain traces of Pb but almost no U or Th, such as pyrite, sphalerite and chalcopyrite (Cheilletz, 1984; Tarrieu, 2014), the most radiogenic ratios observed along trend A likely result from remobilisation of lead from these magmatic sulphides at 255 Ma. Concerning trend B, the most radiogenic Pb ratios ($^{207}Pb/^{204}Pb = 15.80$) likely, result from leaching of highly radiogenic upper crustal rocks. As the upper crust is mainly composed of Paleozoic formations (black schists and limestones) and Permian sediments at the time of the Pb-Zn-Ag ore precipitation, these rocks likely provide the high radiogenic lead isotope signature. Even thought, more data would be required in order to confirm this hypothesis, Pb inheritance from the country rocks has been evidenced in many Pb deposits (e.g., Marcoux and Moëlo, 1991).

Pb isotope data thus indicate a complex system, involving a deep source of lead (mantle and/or lower crust) and remobilisation of Variscan lead at 255 Ma (trend A), together with mobilisation of more radiogenic crustal lead at 255 Ma (trend B).

5. Discussion

5.1. Metal and fluid sources

Datasets obtained by combining various analytical methods indicate no crystallographic, paragenetic or vein control, suggesting that the Pb-Zn-Ag mineralization of the polymetallic Tighza district

crustallized from a single hydrothermal event, with the four paragenetic sequences highlighting the reactive fluid evolution in time.

The geochemical data clearly indicate that the W-Au and the Pb-Zn-Ag ores precipitated from different fluid sources. The hydrothermal fluid related to the W-Au ores derived from coeval magmatism (e.g., Cheilletz and Zimmerman, 1982; Giuliani et al., 1987; Marcoux et al., 2015), with a contribution of 20 to 30 %, of mantle-derived fluids evidenced in this study from He isotopes, as well as mixing with some meteoric fluids (Ar isotopes; Figure 13B). On the contrary, all geochemical data from this study and from the literature converge and indicate that the Pb-Zn-Ag mineralization is associated with a complex hydrothermal system involving various lead and fluid reservoirs (Figure 13C), with (i) an important crustal component evidenced by REE in gangue carbonates as well as He, O, C, Nd and Pb isotopes, (ii) a meteoric component evidenced by Ar isotopes, and (iii) a deep source (mantle or lower crust) evidenced by Pb isotopes. As shown from O-C, Nd and Pb isotopes, the crustal component likely reflects at least two crustal reservoirs with varying contributions: the late-Carboniferous granitic stocks and the Paleozoic metasediments. Even though the involvement of the two crustal reservoirs and the meteoric source have already been proposed by Castorina and Masi (2000, 2008) using Sr and Nd analyses on siderites from Signal and Sidi Ahmed veins, this study confirms and strengthens the hydrothermal model and presents the first evidence for the implication of a deeper source (mantle and/or lower crust). Permo-triassic dikes have high-K calc-alkaline signature that reflects either an enriched mantle or a lower crustal component (Gasquet and Bouloton, 1995; Youbi et al., 1996), which is consistent with this deep reservoir being the source of Permo-triassic magmatism. However, as He data show no evidence of any significant mantle contribution for the Pb-Zn-Ag mineralization, the deeper source evidenced from relatively unradiogenic Pb ratios in Figure 12 most likely represent a contribution of lower crustal rocks. Therefore, the hydrothermal fluid associated with the Pb-Zn-Ag deposit has a strong crustal component and results from mixing of crustal fluids, magmatic fluids (likely derived from lower crust anatexis, see below) and meteoric fluids. The resulting complex reactive fluid is compatible with fluid inclusion data from Nerci (2006) and Marcoux et al. (2015) who evidenced Na-Ca brines as well as a complex fluid implying organic compounds. A more detailed study would be required in order to determine the importance of the Permo-triassic magmatic fluids relative to the other crustal fluids.

The occurrence of late P4-calcite (group 2) with distinct REE+Y patterns than gangue carbonates of group 1 and the presence of synchysite as the main REE-bearing phase in gangue carbonates provide evidence of a later hydrothermal alteration of primary monazite and xenotime from H_2O-CO_2-F-rich fluids (Förster, 2001).

5.2. Genetic consideration and geodynamic implications

Rossi et al (2016) demonstrated that at least three successive magmatic-hydrothermal events occurred in the TJAD between late-Carboniferous and middle-Triassic (Figure 13):

1- Late-Carboniferous magmatic activity produced first the outcropping granitic stocks (320-300 Ma, Figure 13A; Tarrieu, 2014; Cheilletz et al., 2015; Rossi et al., 2016).

2- The W-Au deposit results from a magmatic-hydrothermal event at 295-280 Ma (Cheilletz and Zimmerman, 1982; Watanabe 2002; Cheilletz et al., 2015; Marcoux et al., 2015; Rossi et al., 2016) that is related to the intrusion of a thin and shallow hidden pluton (Figure 13B; El Dursi, 2009). The related hydrothermal fluid has a strong magmatic origin (Marcoux et al., 2015), with a significant mantellic component, which is consistent with the late-Carboniferous high-K calc-alkaline magmatism having a deep source (Gasquet et al., 1996; El Hadi et al., 2006). This hydrothermal fluid was mixed with meteoric fluids (Figure 13B). The late-Carboniferous and Permian extensional tectonics induced a crustal thinning (Michard et al., 2008; and references therein) and melting of the underlying mantle and lower crust to produce calc-alkaline magmas (Gasquet et al., 1996; El Hadi et al., 2006). Magma emplacement generated high-temperature hydrothermal fluids that mobilized metals from the surrounding rocks (Marcoux et al., 2015), produced a hydrothermal alteration halo (Cheilletz, 1984; Cheilletz and Isnard, 1985) and lead to W-Au precipitation at high temperature. As proposed by Marcoux et al. (2015), the W-Au mineralization can thus be considered as an intrusion-related gold deposit. In addition, due to the occurrence of large dissemination patterns, W-rich skarn, stockwerks, sheated veins and large W-Au veins, this deposit can also be considered as a porphyry-type deposit, in an extensional context (e.g., Seedorff et al., 2005).

3- Dating of the Pb-Zn-Ag mineralization at 254 ± 16 Ma indicate that this hydrothermal event is clearly disconnected with, but superimposed to the W-Au mineralization between late-Permian and Middle Triassic (Tarrieu, 2014; Cheilletz, et al., 2015; Rossi et al. 2016). During that period, the extensional tectonic regime and crustal thinning intensifies, and magmatic activity evolves from plutonic to hypovolcanic in the TJAD (Agard et al., 1958; Cheilletz, 1984; Youbi et al., 1995; Tarrieu, 2014; Rossi et al., 2016). Reactivation of the old dextral crustal-scale shear zones in a sinistral tectonic regime leads to opening of SW-NE tension-gashes that channel magmas and hydrothermal fluids (Figure 2). The emplacement of a dense network of high-K calc-alkaline to alkaline dikes increases the regional heat flux, which triggers circulation of hydrothermal crustal fluids. During fluid flow, these fluids leached the upper crustal rocks, including the Paleozoic metasediments, late-Carboniferous granites and possibly the Permian detrital sediments (Figure 13C). Mixing with meteoric fluids occurred, as well as various degrees of mixing with Permo-triassic magmatic fluids. The Pb-Zn-Ag mineralization can be considered an epithermal vein-type as it developed in association to high-K calc-alkaline to alkaline volcanic activity (Youbi et al., 1995; Tarrieu, 2014; Rossi et al., 2016), under rather low temperatures ($T > 230°C$; Nerci, 2006; Marcoux et al., 2015), at shallow crustal levels (Youbi et al., 1995), and mostly involved hydrothermal crustal fluids.

The occurrence of a later hydrothermal event is evidenced in the TJAD by a change in REE+Y pattern of late calcite, and by the alteration of primary monazite and xenotime into synchysite. This reaction involves circulation of late H_2O-CO_2-F-rich fluids. Similar fluids have been described in the

neighboring El Hammam deposit (dated at 205 ± 1 Ma by Cheilletz et al., 2010; Zemri et al., 2015), the Zrahina deposit, which is assumed to be Permo-triassic in age from field observations (Jébrak, 1982), and the El Aouli deposit (Margoume et al., 2015). The hydrothermal activity that developed during Triassic-Jurassic extensional tectonic regime thus likely affected the Tighza district.

Sb-Ba mineralization is also present in the TJAD, though its age is poorly constrained. Its geochronological and genetic position relative to the two other mineralization events is not known with certainty but is probably younger (Agard et al., 1958).

Radiometric ages of magmatic-hydrothermal activity from Tarrieu (2014) and Rossi et al. (2016) constrain the timing of the model proposed by Marcoux et al. (2015) for the TJAD: the Pb-Zn-Ag mineralization appears to be clearly disconnected from the W-Au mineralization, as it is about 30 Ma younger. Therefore, the model proposed in this paper diverges from Marcoux et al. (2015). For these authors, the Pb-Zn-Ag mineralization is related to fluid focusing at the top of the solidified and cold intrusion that produced the W-Au mineralization. In our model, the Pb-Zn-Ag mineralization is triggered by Permo-triassic magmatic activity due to post-Variscan extensional tectonics. The ore deposits of the TJAD are thus spatially associated with multiple intrusions of Cordilleran-type calc-alkaline magmatism (cf., Sillitoe 2010; Catchpole 2011). Fluid flow and related polymetallic mineralization were generated during a late-Variscan to Permo-Triassic transpressional regime (Michard et al., 2008) that favoured the development of mantle and crust-derived magmas. These two events belong to a key period between the end of the Variscan belt formation in Morocco and the beginning of the Atlantic Ocean opening in the region as highlighted by Liassic volcanism of the CAMP (Mahmoudi and Bertrand, 2007; Verati et al., 2007, Margoum et al., 2015).

The occurrence of hydrothermal and magmatic activity during Permian and Triassic times was not limited to the Moroccan Meseta. The Aouli Pb-Zn veins from the Upper Moulouya district (Eastern Mesesta, Morocco) formed in a similar context to the Tighza Pb-Zn-Ag ore. According to Jébrak et al., (1998) and Margoum et al., (2015), lead was leached from neighbouring Variscan granites and from underlying Proterozoic rocks between 250 and 210 Ma. The Aouli deposit thus seems to be nearly contemporaneous with the Tighza Pb-Zn-Ag event. In the Central Pyrenees, several Pb-Zn-Ag vein-type deposits are associated with Permo-Triassic hydrothermal activity that resulted in lead leaching from the surrounding bedrock and remobilization from previously formed Pb-rich ore deposits (e.g., Munoz et al., 2015; Subías et al., 2015; and references therein). As shown from Pb isotopic signatures of the Pb-Zn-Ag mineralization, similar remobilization of older Pb occurred in the TJAD. Permo-Triassic Pb-Zn-Ag vein-type ores hosted in Variscan basement thus likely result from crustal thinning and resulting melting that preceded the Atlantic Ocean rifting. The occurrence of a deep source of lead has only been observed in the TJAD, probably because of its more westward location (Murphy et al., 2016). Indeed, at 250-230 Ma, the continental crust was the most thinned in the vicinity of the future rift axis, so that melting affected deeper crustal levels (e.g., Tighza district) than further East (e.g., upper Moulouya in Central Morocco and Pyrenean deposits).

The model proposed for the TJAD is actually consistent with other Pb-Zn-Ag(-F) deposits of similar age or geological context (extensional and transcurrent tectonic regime, reactivation of crustal-scale faults and shear zones, etc.) that are hosted in Palaeozoic basement rocks such as Freiberg (Germany), Harz (Germany) and Coeur d'Alene (Idaho). As for the TJAD, the genesis of these deposits also involves fluid mixing of a deep-seated hydrothermal fluid, with crustal fluids and meteoric fluids under low temperatures (250-300°C), in disconnection with the local plutonic rocks (e.g., Beaudoin and Sangster, 1992; Paiement et al., 2012).

6. Concluding remarks

The combination of several isotopic methods provided key data to unravel the complexity of the hydrothermal system associated with the Pb-Zn-Ag mineralization of the TJAD. The multi-proxy approach better constrains the various lead and fluid sources for the Pb-Zn-Ag mineralization. Rare earth elements (REE) content of gangue carbonates, and C-O, Sm-Nd, Ar-He and Pb-Pb isotopic data indicate that the Pb-Zn-Ag mineralization likely resulted from mixing of (i) hydrothermal crustal fluids that interacted with the surrounding late-Carboniferous granites and Paleozoic metasediments, (ii) Permo-triassic magmatic fluids resulting from the melting of lower crustal rocks, and (iii) meteoritic fluids,. The hydrothermal activity and the associated base metal deposits were triggered by Permo-Triassic magmatism produced by the extensional tectonics that pre-dates the Atlantic Ocean opening, which is evidenced by a dense SW-NE-trending magmatic dike network. Therefore, the late-Variscan intrusion-related model must definitively be abandoned to explain the Pb-Zn-Ag ore formation. The polymetallic Tighza-Jbel Aouam district results from the occurrence of a hydrothermal activity related to several magmatic episodes and geodynamic events during late Carboniferous to early Triassic times (Rossi et al., 2016; this study): (1) sterile late-carboniferous felsic intrusion, (2) a reduced intrusion-related W-Au mineralization in early Permian, (3) a Pb-Zn-Ag mineralization triggered by Permo-Triassic magmatic activity in an extensional tectonic regime, (4) later circulation of a H_2O-CO_2-F-rich, possibly late-Triassic in age.

The metallogenic model proposed for the Pb-Zn-Ag Tighza-Jbel Aouam deposit provides new constraints for Pb-Zn-Ag exploration strategies in the Moroccan Meseta. Exploration targets must take into account the following discriminant geological features: (i) Permo-triassic high-K calk-alkaline to alkaline dikes, (ii) extensional tectonics and reactivation of ancient crust-scale faults or shear zones, (iii) Paleozoic metasediments containing organic matter (e.g., black shales) subjected to low grade metamorphism (e.g., greenschist facies).

Acknowledgments

This study was supported by INSU-CNRS through the CESSUR program, by a collaboration agreement between Université Savoie Mont Blanc and the Compagnie Minière de Touissit (CMT). It

was part of Leïla Tarrieu's PhD at the University of Savoie-Mont-Blanc, supported by the French Ministry for Research and Higher Education. This paper is dedicated to the memory of Pete Burnard, who passed away in 2015, and who provided the Ar-He data and thus contributed to better understanding the fluid sources of the polymetallic district of Tighza-Jbel Aouam. The authors are thankful to Mohammed Bouabdellah for his constructive remarks that help improving this manuscript, and to an anonymous reviewer.

References

Agard, J., Balcon, J.M., Morin P., 1958. Etude géologique de la région minéralisée du Jebel Aouam (Maroc central). Notes Mémoires Service Géologique Maroc 132, 127.

Andrews, J.N., 1985. The isotopic composition of radiogenic helium and its use to study groundwater movement in confined aquifers. Chemical Geology 49, 339-351.

Arribas, A.Jr., Tosdal, R.M., 1994. Isotopic composition of Pb in ore deposits of the Betic Cordillera, Spain: origin and relationship to other European deposits. Economic Geology 89, 1074-1093.

Bamoumen, H., Aarab, M. Soulaimani, A., 2008. Evolution tectono-sédimentaire et magmatique des bassins viséen supérieur d'Azrou-Khenifra et des Jebilet orientales (Meseta marocaine). Estudio Geologicos 64 (2), doi:10.3989/egeol.08642.020.

Bau, M., 1991. Rare-earth element mobility during hydrothermal and metamorphic fluid–rock interaction and the significance of the oxidation state of europium. Chemical Geology 93, 219-230.

Bau, M., Möller, P., 1992. Rare earth element fractionation in metamorphogenic hydrothermal calcite, magnesite and siderite. Mineralogy and Petrology 45, 231-246.

Beaudoin, G., Sangster, D.F., 1992. Descriptive model for Silver-Lead-Zinc Veins in Clastic Metasedimentary Terranes. Economic Geology 87. 1005-1021.

Bouabdelli, M., Piqué, A., 1996. Du bassin sur décrochement au bassin d'avant-pays: Dynamique du bassin d'Azrou-Khenifra (Maroc hercynien central). Journal of African Earth Sciences 23, 213-224.

Bouabdellah, M., Beaudoin, G., Leach, D.L., Grandia, F., Cardellach, E., 2009. Genesis of the Assif El Mal Zn-Pb (Cu-Ag) vein deposit. An extension-related Mesozoic vein system in the High Atlas of Morocco. Structural, mineralogical and geochemical evidence. Mineralium Deposita 44, 689-704.

Bouabdellah, M., Niedermann, S., Velasco, F., 2015. The Touissit-Bou Beker Mississippi Valley-Type District of Northeastern Morocco: Relationships to the Messinian Salinity Crisis, Late Neogene-Quaternary Alkaline Magmatism, and Buoyancy-Driven Fluid Convection. Economic Geology 110, 1455-1484.

Bouloton, J., Gasquet, D., 1995. Melting and undercooled crystallisation of felsic xenoliths from minor intrusions (Jebilet massif, Morocco). Lithos 35, 201-219.

Boushaba, A., Marignac, C., 2009. La nature des fluides hydrothermaux des tourmalinites du massif granitique permien du Ment (Maroc central) : couplage de la mineralogie des tourmalines et de l'étude des inclusions fluides. Collection EDYTEM 9, 33-48.

626 Boutaleb, M., 1988) Reconstitution de l'évolution tectono-métamorphique, magmatique et
627 hydrothermale du district stanno-wolframifère de Walmès (Maroc central). Implications
628 métallogéniques. PhD thesis, INPL, Nancy, 268 p.
629 Burnard, P.G., Hu, R., Turner, G., Br, X.W., 1999. Mantle, crustal and atmospheric noble gases in
630 Ailaoshan Gold deposits, Yunnan Province, China. Geochimica et Cosmochimica Acta 63(10),
631 1595-1604.
632 Burnard, P.G., Polya, D.A., 2004. Importance of mantle derived fluids during granite associated
633 hydrothermal circulation: He and Ar isotopes of ore minerals from Panasqueira. Geochimica and
634 Cosmochimica Acta 68(7), 1607-1615.
635 Campbell, A., Larson, P., 1998. Introduction to stable isotope applications in hydrothermal ore
636 deposits. Reviews in Economic Geology 6, 173-193.
637 Castorina, F., Masi, 2000. Sr-isotopic composition of siderite for assessing the origin of mineralizing
638 fluids: the case study from the Jebel Awam deposit (Central Morocco). Ore Geology Reviews 17,
639 83-89.
640 Castorina, F., Masi, U., 2008. REE and Nd-isotope evidence for the origin of siderite from the Jebel
641 Awam deposit (Central Morocco). Ore Geology Reviews 34, 337-342.
642 Catchpole, H.P., 2011. Porphyry-related polymetallic mineralisation in the Morococha district, central
643 Peru: mineralisation styles, timing and fluid evolution. PhD thesis, Genève University, Switzerland,
644 288p.
645 Chacko, T., Mayeda, T.K., Clayton, R.N., Goldsmith, J.R., 1991. Oxygen and carbon isotopic
646 fractionation between CO_2 and calcite. Geochimica et Cosmochimica Acta 55, 2867-2882.
647 Cheilletz, A., 1984. Contribution à la gîtologie du district polymétallique (W-Mo-Cu-Pb-Zn-Ag) du
648 Djebel Aouam (Maroc central): application à la prospection des gisements de tungstène. Doctorat
649 d'Etat, Institut National Polytechnique de Lorraine, France, 273 p.
650 Cheilletz, A., Zimmermann, J.L., 1982. Datations par la méthode K-Ar du complexe intrusif et des
651 minéralisations en tungstène du Jbel Aouam (Maroc central). Comptes Rendus Académie Sciences,
652 Série II, 295, 255–258.
653 Cheilletz, A., Isnard, P., 1985. Contribution à la prospection des gisements hydrothermaux de
654 tungstène sur l'exemple du district polymétallique W-Pb-Zn-Ag du Jbel Aouam (Maroc central).
655 Mineral Deposita 20, 220-230
656 Cheilletz, A., Gasquet, D., Filali, F., Archibald, D.A., Nespolo, M., 2010. A Late Triassic $^{40}Ar/^{39}Ar$
657 age for the El Hamman high-REE fluorite deposit (Morocco): mineralization related to the Central
658 Atlantic Magmatic Province? Mineral Deposita 45, 323-329.
659 Cheilletz, A., Rossi, M., Tarrieu, L., Gasquet, D., Bounajma, H., Mantoy, T., Ouazzani, L.,
660 Ouchtouban, L., Deloule, E., Burnard, P., Paquette, J.L., 2015. A cordilleran zoning model for the
661 polymetallic W-Au-Pb-Zn-Ag Tighza-Jbel Aouam District (Central Morocco): contribution from

new He-Ar and U-Th-Pb data. Proceedings of the 13th SGA meeting, Nancy (France), vol. 4, 1579-1582.

Deloule, E., Allègre, C.J., Doe, B., 1986. Lead and sulfur isotope microstratigraphy in galena crystals from Mississippi-Valley type deposits. Economic Geology 81, 1307-1321.

Desteucq, C., 1974. Le système filonien du Jbel Aouam (Maroc central); essai d'interprétation structurale. PhD thesis, University Paul Sabatier, Toulouse, France, 93p.

El Dursi, K., 2009. Minéralisations et circulations péri-granitiques: modélisation numérique couplée 2D/3D, applications au district minier de Tighza (Maroc central). PhD thesis, Univerity Orléans, France, 218p.

El Hadi, H., Simancas, J.F., Tahiri, A., Gonzalez Lodeiro, F., Azor, A., Martinez Poyatos, D., 2006. Comparative review of the Variscan granitoids of Morocco and Iberia: proposal of a broad zonation. Geodinamica Acta 19(2),103-116.

Faure, G., Mensing, T.M., 2005. Isotopes: principles and applications. Third edition, Wiley (ed.), 897p.

Field, C., Fifarek, R., 1985. Light stable-isotope systematics in the epithermal environment. Review in Economic Geology 2, 99-128.

Fontes, J.C., Andrews, J.N., Walgenwitz, F., 1991. Evaluation de la production naturelle in situ d'argon-36 via le chlore-36; Implications geochimiques et geochronologiques: Evaluation of natural in situ production of argon-36 via chlorine-36; Geochemical and geochronological implications. Comptes Rendus de l'Academie des Sciences, Serie IIA 313, 649-654.

Förster, H.J., 2001. Synchysite-(Y) - synchisite-(Ce) solid solutions from Markersbach, Erzgebirge, REE and Th mobility during high-T alteration of highly fractionated aluminous A-type granites. Mineralogy and Petrology 72(4), 259-280.

Gasquet, D., Bouloton, J., 1995. Les filons de microdiorite des Jebilet centrales (Meseta marocaine): pré-rifting permien ? Rés. Réun. extraord. Société géologique de France, Marrakech, Abstract book, 55.

Gasquet, D., Stussi, J.M., Nachit, H., 1996. Les granitoïdes hercyniens du Maroc, dans le cadre de l'évolution géodynamique régionale. Bulletin Société géologique de France 167(4), 517-528.

Gasquet, D., Ennih, N., Liégeois, J.P., Soulaimani, A., Michard, A., 2008. The Pan-Arican belt. In : Michard et al., Continental Evolution: The geology of Morocco. Lecture notes in Earth Sciences 116, Springer Verlag Ed, 33-64.

Giuliani, G., Cheilletz, A., Mechiche, M., 1987. Behaviour of REE during thermal metamorphism and hydrothermal infiltration associated with skarn and vein-type tungsten ore bodies in central Morocco. Chemical Geology 64, 279-294.

Giuliani, G., Cheilletz, A., Zimmermann, J.L., 1989. The emplacement, geochemistry and petrogenesis of two central Morocco Hercynian granites. Geotectonic implications. Journal of African Earth Sciences 9, 617-629.

Guilbert, J.M., Park, C.F.Jr., 1999. The geology of ore deposits. Freeman and Co. (ed.), 985p.

699 Hecht, L., Freiberger, R., Gilg, HA., Grundmann, G., and Kostitsyn, Y.A., 1999, Rare earth element
700 and isotope (C,O,Sr) characteristic of hydrothermal carbonates: Genetic implications for dolomite-
701 hosted talc mineralization at Göpfersgrün (Fichtelgebirge, Germany). Chemical Geology 155, 115-
702 130.
703 Jacobsen, S.B.,Wasserburg, G.J.,1980. Sm–Nd isotopic evolution of chondrites. Earth and Planetary
704 Science Letters 50, 139-155.
705 Jébrak, M., 1982. Les districts à fluorine du Maroc Central. Bulletin du BRGM II, 211-221.
706 Jébrak, M., 1984. Contribution à l'histoire naturelle des filons (F-Ba) du domaine Varisque français et
707 marocain. Essai de caractérisation structurale et géochimique des filons en extension et en
708 décrochement dans les massifs centraux français et marocains. Doctorat d'Etat, University of
709 Orléans, France, 467p.
710 Jébrak, M., 1985. Le district filonien à Pb-Zn-Ag et carbonates du Jebel Aouam (Maroc Central).
711 Bulletin de Minéralogie 108, 487-498.
712 Jébrak, M., Marcoux, E., Nasloubi, M., Zaharaoui, M., 1998. From sandstone- to carbonate-hosted
713 stratabound deposits: an isotope study of galena in the upper-Moulouya District (Morocco).
714 Mineralium Deposita 33, 406-415.
715 Jones, A., Genge, M., Carmody, L., 2013. Carbonate melts and carbonatites. In: Carbon in Earth,
716 Hazen, RM and Jones, AP and Baross, JA, (eds.) Ed. Mineralogical society of America, 280-322.
717 Kendrick, M.A., Burgess, R., Harrison, D., Bjorklykke, A., 2005. Noble gas and halogen evidence for
718 the origin of Scandinavian sandstone-hosted Pb-Zn deposits. Geochimica et Cosmochimica Acta 69,
719 109-129.
720 Kharaka, Y., Hanor, J., 2003. Deep Fluids in the Continents: I. Sedimentary Basins. Treatise on
721 Geochemistry 5, 1-48.
722 Lüders, V., Möller, P., Dulski, P., 1993. REE fractionation in carbonates and fluorites. In: Möller, P.,
723 and Lüders, V., eds., Formation of hydrothermal vein deposits: Berlin-Stuttgart, Gebrüder
724 Borntträeger, Monograph Series on Mineral Deposits 30, 133-150.
725 Ludwig, K.R., Vollmer, R., Turi, B., Simmons, K.R., Perna, G., 1989. Isotopic constraints on the
726 genesis of base-metal ores in southern and central Sardinia. European Journal of Mineralogy, 1,
727 657–666.
728 Mahmoudi, A., Bertrand, H., 2007. Identification géochimique de la province magmatique de
729 l'Atlantique central en domaine plissé : exemple du Moyen Atlas marocain. C. R. Geoscience 339,
730 545-552.
731 Marcoux, E., Moëlo, Y., 1991. Lead isotope geochemistry and paragenetic study of inheritance
732 phenomena in metallogenesis: examples from base metal sulfide deposits in France. Economic
733 Geology 86, 106-120.

Marcoux, E., Nerci, K., Branquet, Y., Ramboz C., Ruffet, G., Peucat, J.J., Stevenson, R., Jebrak, M., 2015. Late-Hercynian Intrusion-related gold deposits: an integrated model on the Tighza polymetallic district, central Morocco. Journal of African Earth Science 107, 65-88.

Margoum, D., Bouabdellah, M., Klügel, A., Banks, D.A., Castorina, F., Cuney, M., Jébrak, M., Bozkaya, G., 2015. Pangea rifting and onward pre-Central Atlantic opening as the main ore-forming processes for the genesis of the Aouli REE-rich fluorite–barite vein system, Upper Moulouya District, Morocco. Journal of African Earth Sciences 108, 22-39.

Marignac, C., Cuney, M., 1999. Ore deposits in the French Massif Central: insight into the metallogenesis of the Variscan collision belt. Mineralium Deposita 34, 472-504.

Marty, B., Zimmermann, L., 1999. Volatiles (He, C, N, Ar) in mid-ocean ridge basalts: assessment of shallow-level fractionation and characterization of source composition. Geochimica et Cosmochimica Acta 63(21), 3619-3633.

McLennan, S.M., 1989. Rare earth elements in sedimentary rocks: influence of provenance and sedimentary processes. Reviews in Mineralagy 21, 169-200.

Michard, A., 1989. Rare-earth element systematics in hydrothermal fluids. Geochimica et Cosmochimica Acta 53, 745-750.

Michard, A., Hoepffner, C., Soulaimani, A., Baidder, L., 2008. The Variscan belt. In: Michard, A., Saddiqi, O., Chalouan, A., Frizon de Lamotte, D. (eds) Continental evolution: the geology of Morocco. Lecture Notes Earth Sci 116, Springer-Verlag, Berlin-Heidelberg, 65-132.

Möller, P., Lüders, V., Schröder, J., Luck, J., 1991. Element partitioning in calcites as a function of solution flow rate: a study on vein calcites from the Harz Mountains. Mineralium Deposita 26, 175-179.

Munoz, M., Baron, S., Boucher, A., Béziat, D., Salvi, S., 2015. Mesozoic vein-type Pb–Zn mineralization in the Pyrenees: Lead isotopic and fluid inclusion evidence from the Les Argentie` res and Lacore deposits. C.R. Géosciences, serie 2, http:// dx.doi.org/10.1016/j.crte.2015.07.001.

Murphy, J.B., Quesada, C., Gutiérrez-Alonso., G., Johnston, S.J., Weil, A., 2016. Reconciling competing models for the tectonostratigraphic zonation of the Variscan orogen in western Europe, Tectonophysics, doi: 10.1016/j.tecto.2016.01.006.

Nerci, K., 2006. Les minéralisations aurifères du district polymétallique de Tighza (Maroc central): un exemple de mise en place périgranitique tardihercynienne. PhD thesis, Université d'Orléans – Université du Québec à Montréal, 302 p.

Paiement, J-Ph., Beaudoin, G., Paradis S. and Ullrich, T., 2012. Geochemistry and metallogeny of Ag-Pb-Zn veins in the Purcell Basin, British Columbia. .Economic Geology 107, 1303–1320.

Pereira, M.F., El Houicha, M., Chichorro, M., Armstrong, R., Jouhari, A., El Attari, A., Ennih, N., Silva, J.B., 2015. Evidence of a Paleoproterozoic basement in the Moroccan Variscan Belt (Rehamna Massif, Western Meseta). Precambrian Research 268, 61-73.

Pin, C., Zalduegui, J.F.S., 1997. Sequential separation of light rare-earth elements, thorium and uranium by miniaturized extraction chromatography: Application to isotopic analyses of silicate rocks. Analytica Chimica Acta 339, 79-89.

Piqué, A., Soulaimani, A., Hoepffner, C., Bouabdelli, M., Laville, E., Amrhar, M., Chalouan, A., 2007. Géologie du Maroc, Ed. Géode, Marrakech, 287p.

Porcelli, D. R., O'Nions, R. K., Galer, S.G., Cohen, A.S., Mattey, D. P., 1992. Isotopic relationships of volatile and lithophile trace elements in continental ultramafic xenoliths. Contribution Mineralogy and Petrology 110, 528-538.

Rollinson, H., 1993. Using geochemical data: Evaluation, presentation, interpretation, 352p.

Rossi. M., and Tarrieu, L., Cheilletz, A., Gasquet, D., Deloule, E., Paquette, J.L., Bounajma, H., Mantoy, T., Ouazzani, L., Ouchtouban, L., 2016 The polymetallic (W-Au/Pb-Zn-Ag) Tighza district (central Morocco): age of the magmatic and hydrothermal events. In: Bouabdellah, M., and Slack, J.F., eds., Mineral deposits of North Africa: Berlin-Heidelberg, Springer-Verlag. DOI: 10.1007/978-3-319-31733-5_6.

Saadi, M., 1982. Carte structurale du Maroc (1/2 000 000). Notes et mémoires du service géologique du Maroc.

Schaltegger, U., Stille, P., Rais, N., Piqué, A., Clauer, N., 1994. Neodymium and strontium isotopic dating of diagenesis and low-grade metamorphism of argillaceous sediments. Geochimica et Cosmochimica Acta 58, 1471-1481.

Seedorff, E., Dilles, J.H., Proffet, J.M., Enaudi, M.T., 2005. Porphyry deposits: characteristics and origins of hypogene features. In: Economic Geology 100th Anniversary volume, 251-298.

Sillitoe, R.H., 2010. Porphyry-copper systems. Economic Geology 105, 3-41.

Stacey, J.D., Kramers, J.D., 1975. Approximation of terrestrial lead isotope evolution by a two-stage model. Earth Planetary Science Letters 26, 207–221.

Steiger, R.H. and Jäger, E., 1977. Subcommission on geochronology: Convention on the use of decay constants in geo- and cosmochronology. Earth and Planetary Science Letters 36(3), 359-362.

Subías, I., Fanlo, I., Billström, K., 2015. Ore-forming timing of polymetallic-fluorite low temperature veins from Central Pyrenees: a Pb, Nd and Sr isotope perspective. Ore Geology Reviews 70, 241-251.

Tarrieu, L., 2014. Nouvelles données minéralogiques, géochimiques et géochronologiques sur le gisement polymétallique de Tighza (Maroc Central) – Contribution à la métallogénie des géisements de métaux de base filoniens en contexte post-collisionnel. PhD thesis, Univerity of Savoie, France, 240p.

Tartèse, R., Boulvais, P., Poujol, M., Chevalier, T., Paquette, J-L., Ireland, T., Deloule, E., 2012. Mylonites of the South Armorican Shear Zone: Insight for crustal-scale fluid flow and water-rock interaction processes. Journal of Geodynamics 56, 86-107.

Torres-Ruiz, J., 2006. Geochemical constraints on the genesis of the Marquesado iron ore deposits, Betic Cardillera, Spain: REE, C, O and Sr isotope data. Economic Geology 101, 667-677.

Verati, C., Rapaille, C., Feraud, G., Marzoli, A., Bertrand, H., Youbi, N., 2007. $^{40}Ar/^{39}Ar$ ages and duration of the Central Atlantic Magmatic Province volcanism in Morocco and Portugal and its relation to the Triassic-Jurassic boundary. Palaeogeography, Palaeoclimatology, Palaeoecology 244, 308–325.

Wadjinny, A., 1998. Le plomb au Maroc: cas des districts de Touissit et de Jbel Aouam. Chroniques de la Recherche Minière 531-532, 9-28.

Watanabe, Y., 2001. Timing of volcano-sedimentary massive sulfide and vein-type Pb-Zn mineralization in the western meseta of Morocco: ^{40}Ar-^{39}Ar geochronology. Exploration Technology and interpreting methods Part IV, JICA-B.R.P.M project (1998-2002).

Watanabe, Y., 2002. $^{40}Ar/^{39}Ar$ Geochronologic constraints on the timing of massive sulfide and vein-type Pb-Zn mineralization in the Western Meseta of Morocco. Economic Geology 97, 145-157.

Williams-Jones, A.E., Migdisov, A.A., Samson, I.M., 2012. Hydrothermal mobilization of the rare earth elements – a tale of "Ceria" and "Yttria". Elements 8, 355-360.

Youbi, N., Cabanis, B., Chalot-Prat, F., Cailleux, Y., 1995. Histoire volcano-tectonique du massif permien de Khénifra (Sud-Est du Maroc Central). Geodinamica Acta (Paris) 8 (3), 158-172

Zartman, R.E., Haines, S.M., 1988. The plumbotectonic model for Pb-isotopic systematics among major terrestrial reservoirs – A case for bi-directional transport. Geochimica et Cosmochimica Acta 52, 1327-1339,

Zemri, O., Bouabdellah, M., Jébrak, M., Sadequi, M., Gaouzi, A., Maacha, L., 2015. Geology and REE geochemistry of the El Hammam REE-rich fluorite deposit (Central Meseta, Morocco). Proceedings of the 13th SGA meeting, 1679-1682.

Zheng, Y.F., 1999. Oxygen isotope fractionation in carbonate and sulfate minerals, Geochemical Journal 33, 109-126.

Figure captions

Figure 1. A) Simplified geological map of central Morocco (modified from Youbi et al., 1995). B) Structural map of the Azrou-Khenifra basin in the Central Meseta (modified from Saadi, 1982; Bouabdelli and Piqué, 1996; Bamoumen et al., 2008).

Figure 2. Geological map of the polymetallic Tighza district in central Morocco. Modified from Agard et al. (1958), Cheilletz (1984), and CMT (pers. comm. 2013).

Figure 3. Relationships between Pb-Zn-Ag and W-Au mineralization: Pb-Zn-Ag veins cut W-Au veins in the roof of Structure 18.

Figure 4. A) Underground photograph showing banded mineralized vein from Filon Signal (sub-level 13). B) Brecciated and banded Pb-Zn-Ag veins in Sidi Ahmed. P1, P2, P3 and P4 refer to the successive paragenetic sequences in Figure 5.

Figure 5. Paragenetic sequence of the Pb-Zn mineralisation. SA and IA stand for Sidi Ahmed and Ighrem Aousser veins respectively.

Figure 6. REE total content of undifferentiated gangue carbonates from Tighza Pb-Zn-Ag veins. Data from this study, Jébrak (1985) and Castorina and Masi (2008).

Figure 7. PAAS-normalized REE patterns of gangue carbonates from the main Pb-Zn-Ag veins of Tighza district. Magmatic rock data from this study and from Giuliani et al., 1987). REE patterns of carbonates from the El Hammam F-deposit are indicated for comparison (data from Cheilletz et al., 2010; Zemri et al., 2015). PAAS normalization values from McLennan (1989).

Figure 8. REE-bearing phases hosted in gangue carbonates. A) and B) SEM pictures of synchysite crystals hosted in gangue calcite. C) EDS spectra of synchysite. D) Ce-La-Y Ternary diagram showing the composition of some synchysite crystals hosted in P4 calcite from Sidi Ahmed (Tz10/25) and Ighrem Aousser (Tz10/32, Tz10/28).

Figure 9. Carbon and oxygen isotopic signatures of gangue carbonates from the Pb-Zn-Ag mineralization (circles) and of a H_2O-rich fluid in equilibrium with the carbonates at 230°C (squares; see text for explanation). The isotopic ranges of terrestrial reservoirs are reported from Field and Fifarek (1985), Rollinson (1993), Campbell and Larson (1998), Kharaka and Hanor (2003), Tartèse et al., (2012) and Jones et al. (2013).

Figure 10. ε_{Nd} of gangue carbonates, magmatic rocks and Paleozoic sediments at the time of Pb-Zn-Ag ore formation (i.e., at 255 Ma; Rossi et al., 2016). $\varepsilon_{Nd\text{-}255Ma}$ values of local siderites have been estimated using data from Castorina and Masi (2008), $\varepsilon_{Nd\text{-}255Ma}$ values of magmatic rocks have been estimated using data from Castorina and Masi (2008) and Marcoux et al. (2015), and $\varepsilon_{Nd\text{-}255Ma}$ values of Paleozoic rocks have been estimated using data from Castorina and Masi (2008; local rocks) and Schaltegger et al. (1994; moroccoan Cambrian schists). $\varepsilon_{Nd\text{-}255Ma}$ of moroccoan Cambrian schists are in the same range as Paleozoic schists from the Tighza district.

Figure 11. $^{40}Ar/^{36}Ar$ and $^{3}He/^{4}He$ (normalized to the atmospheric $^{3}He/^{4}He$ ratio) of sulphide minerals from W-Au (green) and Pb-Zn-Ag (red) deposits from Tighza district. Both deposits display meteoric Ar signatures but distinct He signatures: while Pb-Zn-Ag ores have crustal He, the W-Au ores evidence mixing with some mantle-derived He. Isotope ratios of the main geological reservoirs f from Steiger and Jäger (1977), Andrews (1985), Fontes et al., (1991), Porcelli et al., (1992), Burnard et al. (1999) and Burnard and Polya (2004).

Figure 12. Pb/Pb isotopic signatures of Pb-Zn-Ag veins, W-Au disseminations and granitoids from this study, Watanabe (2001), Nerci (2006) and Marcoux et al. (2015). Note that the W-Au trend differs from that of Pb-Zn-Ag.

Figure 6. Metallogenic model of the Tighza polymetallic district. The three main hydrothermal events have been identified using U-Pb dating of zircon and Th-U dating of monazite (Rossi et al., 2016). A) Crystallization of the outcropping granitic stocks at 320-300 Ma. B) Deposit of the W-Au ores in

relation with a hidden pluton at 300-280 Ma.. C) Deposit of the Pb-Zn-Ag ores in relation with Permian magmatism at 254 ± 16 Ma. SA, Sidi Ahmed; IA, Ighrem Aousser; S18, Structure 18; FN, Filons Nord; F.P, Filons Parallèles.

Table captions

Table 1. REE pattern of gangue carbonate from the different Pb-Zn-Ag veins.

Table 1. C-O isotopic compositions of gangue carbonates from the Pb-Zn-Ag ore. C-O isotopic compositions of the fluid in equilibirum with gangue carbonates have been calculated using Zheng (1999) and Chacko et al. (1991) thermometers.

Table 3. Sm and Nd contents and ε_{Nd} of the gangue carbonates from the Pb-Zn-Ag deposit of Tighza district.

Table 4. Noble gas compositions of fluids trapped in sulphide minerals from the Tighza polymetallic district.

Table 5. Pb-Pb isotopic ratios of galena.

Table 1. REE contents (ppm) in the carbonates from the Tighza district. Mineral abbreviations from Kretz (1983).

	Paralleles veins			Nord vein	Signal vein	Sidi Ahmed vein						Ighrem Aousser vein										
	Tz11/13.2	Tz11/10	Tz11/13.1	Tz11/67	Tz11/47	Tz10/22	Tz10/17	Tz11/49	Tz11/48	Tz10/25	Tz11/53	Tz10/30.2	Tz10/33	Tz10/33	Tz10/30.1	Tz10/31	Tz10/28	Tz10/29	Tz11/58	Tz10/32	Tz10/34	Tz10/31
					P1	P1	P2	P4	P4	P4	P4	P2	P2	P3	P4	P4	P4	P4	P4	P4	P4	P3
	sid	ank	ank	ank	sid	sid	ank	cal	cal	cal	cal	ankérite	ankérite	sidérite	calcite	calcite	calcite	calcite	calcite	calcite	calcite	calcite
La	6.67	11.22	12.34	11.19	95.94	32.52	14.75	105.20	47.60	107.50	36.23	665.60	12.87	5.22	140.10	132.30	61.47	127.60	38.27	448.40	133.20	322.80
Ce	17.72	56.70	60.37	45.51	174.60	65.15	59.83	138.60	83.85	218.10	61.61	1352.00	49.75	13.75	279.00	282.80	138.10	266.20	62.26	1020.00	275.90	727.00
Pr	2.72	11.45	11.74	8.35	20.42	7.97	9.70	15.29	9.59	28.24	7.19	174.00	8.07	1.92	34.41	36.43	18.74	33.40	6.84	132.40	35.02	92.76
Nd	11.44	55.42	54.99	38.87	87.39	34.63	45.42	65.08	45.58	132.80	34.24	742.70	43.61	9.95	147.60	159.50	91.33	142.40	33.74	538.80	151.90	372.60
Sm	3.64	26.27	24.46	16.19	22.50	9.63	19.31	16.01	13.97	35.53	9.71	262.10	19.50	3.31	44.79	54.37	27.39	41.76	9.17	158.60	50.46	112.00
Eu	1.74	11.99	13.09	7.79	7.98	5.13	6.47	6.66	5.98	4.76	4.22	152.80	8.35	1.89	23.94	29.74	3.01	21.17	5.18	55.98	27.57	42.85
Gd	3.39	25.21	23.61	15.87	21.30	9.07	19.39	20.77	15.17	41.16	10.42	306.70	20.17	3.20	48.24	60.42	34.70	43.15	11.55	162.40	55.69	113.50
Tb	0.52	3.66	3.40	2.18	2.96	1.20	2.63	2.40	2.25	6.65	1.48	41.91	2.73	0.48	7.11	8.41	6.54	6.11	1.57	22.01	8.09	15.29
Dy	2.69	17.44	16.13	10.12	15.69	5.88	11.89	11.11	11.33	41.06	7.30	196.60	12.15	2.41	37.19	40.39	46.54	30.01	7.76	99.44	40.57	66.53
Ho	0.46	2.61	2.41	1.48	2.87	0.96	1.64	1.84	1.87	8.49	1.22	29.08	1.70	0.38	6.27	6.14	11.21	4.87	1.28	13.96	6.57	9.08
Er	1.16	5.94	5.44	3.22	8.60	2.39	3.44	4.27	4.82	23.29	3.04	62.53	3.61	0.92	15.97	14.13	38.44	12.17	3.01	27.83	16.19	18.12
Tm	0.17	0.77	0.71	0.40	1.70	0.36	0.43	0.51	0.69	3.14	0.40	7.37	0.44	0.13	2.33	1.83	7.14	1.68	0.36	2.97	2.29	2.01
Yb	1.19	5.06	4.68	2.61	17.18	2.58	2.79	3.13	4.76	18.84	2.53	42.71	2.88	0.92	16.36	12.65	59.08	11.54	1.98	17.28	16.21	12.88
Lu	0.17	0.71	0.65	0.35	3.22	0.37	0.38	0.48	0.72	2.50	0.36	5.40	0.40	0.13	2.40	1.77	10.13	1.75	0.27	2.30	2.40	1.86
Y	13.31	76.59	70.07	50.44	81.69	28.89	58.38	93.59	64.59	307.8	43.03	1117	57.65	11.83	230.3	239.2	430.2	202.6	50.46	545.5	239.7	391.6
ΣREE	54	234	234	164	482	178	198	391	248	672	180	4041	186	45	806	841	554	744	183	2702	822	1909
Eu/Eu*	2.34	2.19	2.56	2.29	1.72	2.59	1.57	1.72	1.93	0.59	1.98	2.54	1.98	2.73	2.43	2.44	0.46	2.35	2.37	1.64	2.45	1.79
$(La/Yb)_N$	0.41	0.16	0.19	0.32	0.41	0.93	0.39	2.48	0.74	0.42	1.06	1.15	0.33	0.42	0.63	0.77	0.08	0.82	1.43	1.92	0.61	1.85
ΣREE+Y	67	311	304	215	564	207	256	485	313	980	223	5158	244	56	1036	1080	984	946	234	3248	1062	2301
% Y	19.9	24.6	23.0	23.5	14.5	14.0	22.8	19.3	20.7	31.4	19.3	21.7	23.6	21.0	22.2	22.1	43.7	21.4	21.6	16.8	22.6	17.0
% Ce	26.5	18.2	19.9	21.2	31.0	31.5	23.3	28.6	26.8	22.3	27.6	26.2	20.4	24.4	26.9	26.2	14.0	28.1	26.6	31.4	26.0	31.6
% Nd	17.1	17.8	18.1	18.1	15.5	16.8	17.7	13.4	14.6	13.6	15.4	14.4	17.9	17.6	14.2	14.8	9.3	15.0	14.4	16.6	14.3	16.2
% La	10.0	3.6	4.1	5.2	17.0	15.7	5.8	21.7	15.2	11.0	16.2	12.9	5.3	9.2	13.5	12.2	6.2	13.5	16.4	13.8	12.5	14.0
%REE+Y	73.4	64.3	65.0	68.0	77.9	78.0	69.6	83.0	77.3	78.2	78.5	75.2	67.2	72.2	76.9	75.3	73.3	78.1	79.0	78.6	75.4	78.8

Table 2. C-O isotopic compositions of gangue carbonates from the Pb-Zn-Ag ore. C-O isotopic compositions of the fluid in equilibirum with the carbonate have been calculated using Zheng (1999) and Chacko et al. (1991) thermometers.

Stage	Mineral	Sample	$\delta^{18}O_{SMOW}$	$\delta^{13}C_{PDB}$	$\delta^{18}O_{SMOW}$ T = 230°C	$\delta^{13}C_{PDB}$ T = 230°C	$\delta^{18}O_{SMOW}$ T = 280°C	$\delta^{13}C_{PDB}$ T = 280°C
Sidi Ahmed vein								
P1	siderite	Tz10/23	21,3	-5,1	11.9	-3.6	14.0	-2.6
P1	siderite	Tz10/22	21,1	-4,2	11.8	-2.6	13.8	-1.6
P2	ankerite	Tz10/18	21,9	-3,6	13.1	-2.1	15.0	-1.0
P2	ankerite	Tz10/23	24,0	-5,0	15.1	-3.4	17.1	-2.4
P2	ankerite	Tz10/17	19,2	-4,0	10.4	-2.4	12.4	-1.4
P2	ankerite	Tz10/36	20,2	-3,7	11.4	-2.2	13.4	-1.2
P2	ankerite	Tz11/49	21,6	-11,2	13.3	-9.6	15.2	-8.6
P3	siderite	Tz10/18	21,5	-4,5	12.1	-3.0	14.2	-2.0
P4	calcite	Tz11/53	20,3	-8,3	12.0	-6.7	13.9	-5.7
P4	calcite	Tz11/49	22,0	-8,7	13.7	-7.2	15.6	-6.2
P4	calcite	Tz10/25	11,9	-5,7	3.6	-4.1	5.5	-3.1
Ighrem Aousser vein								
P1	siderite	Tz10/29	19,1	-4,5	9.7	-3.0	11.8	-2.0
P2	ankerite	Tz10/30	23,0	-4,1	14.2	-2.6	16.2	-1.6
P2	ankerite	Tz10/33	20,9	-3,8	12.0	-2.3	14.0	-1.3
P3	siderite	Tz10/33	21,4	-4,7	12.1	-3.2	14.2	-2.2
P4	calcite	Tz10/29	20,0	-6,2	11.7	-4.7	13.6	-3.7
P4	calcite	Tz10/31	20,1	-6,2	11.8	-4.7	13.7	-3.7
P4	calcite	Tz10/32	20,3	-6,0	12.0	-4.4	13.9	-3.4
P4	calcite	Tz10/34	19,5	-6,4	11.2	-4.8	13.1	-3.8
P4	calcite	Tz11/58	21,0	-7,3	12.7	-5.8	14.6	-4.8
Signal vein								
P1	siderite	Tz12/01	20,4	-5,1	11.1	-3.6	13.2	-2.6
P2	ankerite	Tz12/02	24,2	-5,3	15.3	-3.8	17.3	-2.7
P4	calcite	Tz10/09	19,0	-2,5	10.7	-1.0	12.6	0.1
P4	calcite	Tz12/01	16,1	-5,8	7.8	-4.3	9.7	-3.2

Table 3. Sm and Nd contents and εNd of the gangue carbonates from the Pb-Zn-Ag deposit of Tighza district.

Stage	Mineral	Sample	[Nd] ppm	[Sm] ppm	$^{143}Nd/^{144}Nd$	$(2\sigma)^a$	$^{147}Sm/^{144}Nd$	εNd_0	$(^{143}Nd/^{144}Nd)_{255\ Ma}{}^b$	$\varepsilon Nd_{255\ Ma}{}^b$	% basement
Sidi Ahmed vein											
P2	ankerite	Tz10/17	30.64	11.94	0.512370	(5)	0.2353	-5.23	0.511977	-6.49	0.53
P2	ankerite	Tz10/22	31.08	8.26	0.512256	(10)	0.1604	-7.45	0.511988	-6.28	0.50
P2	ankerite	Tz11/49	67.11	15.78	0.512201	(2)	0.1419	-8.53	0.511964	-6.76	0.56
P3	calcite	Tz10/25	80.98	23.96	0.512221	(4)	0.1785	-8.14	0.511923	-7.56	0.66
P3	calcite	Tz11/48	46.48	13.55	0.512197	(2)	0.1759	-8.61	0.511903	-7.94	0.71
P3	calcite	Tz11/53	170.91	49.24	0.512246	(4)	0.1739	-7.65	0.511956	-6.91	0.58
Ighrem Aousser vein											
P2	ankerite	Tz10/30.2	303.16	112.91	0.512390	(3)	0.2247	-4.84	0.512015	-5.76	0.44
P2	ankerite	Tz10/31	154.32	48.90	0.512252	(3)	0.1912	-7.53	0.511933	-7.36	0.64
P2	ankerite	Tz10/33.1	8.90	3.14	0.512343	(17)	0.2127	-5.76	0.511988	-6.28	0.50
P2	siderite	Tz10/33.2	42.58	17.87	0.512374	(5)	0.2532	-5.15	0.511951	-7.00	0.59
P3	calcite	Tz11/58	31.98	8.48	0.512206	(3)	0.1601	-8.43	0.511939	-7.24	0.62
P3	calcite	Tz10/28	114.00	26.09	0.512176	(3)	0.1381	-9.01	0.511946	-7.11	0.61
P3	calcite	Tz10/29	130.39	41.51	0.512246	(3)	0.1921	-7.66	0.511925	-7.51	0.66

[a] The figures in parentheses refer to uncertainties of the measurements on the last decimals.

[b] εNd_0 refers to present day; εNd_{255Ma} calculated at the age of the Pb-Zn-Ag formation (Rossi et al., 2016) using the following present-day values for CHUR: $^{147}Sm/^{144}Nd$=0.1966 and $^{143}Nd/^{144}Nd$=0.512638 (Jacobsen and Wasserburg, 1980).

Table 4. Noble gas compositions of fluids trapped in sulphide minerals from the Tighza polymetallic district.

	mineral	vein	mass g	He x 10^{-12} mol/g	$^{3}He/^{4}He$	^{40}Ar x 10^{-12} mol/g	$^{40}Ar/^{36}Ar$	$^{38}Ar/^{36}Ar$
W-Au								
Tz11/23	As-pyrite	W1N	0.500	7.41 ± 0.107	1.814 ± 0.097	7.33 ± 0.286	256 ± 10	0.189 ± 0.013
Tz10/07	As-pyrite	Signal	0.300	8.17 ± 0.117	1.083 ± 0.069	4.08 ± 0.166	304 ± 12	0.181 ± 0.012
Tz10/01	Pyrite	W1N	0.400	4.61 ± 0.069	1.658 ± 0.053	8.77 ± 0.215	328 ± 13	0.168 ± 0.012
Pb-Zn-Ag								
Tz11/35	Pyrite	Sidi Ahmed	0.305	16.3 ± 0.240	0.054 ± 0.005	20.2 ± 0.400	315 ± 12	0.180 ± 0.012
Tz10/53	Pyrite	Sidi Ahmed	0.423	1.42 ± 0.021	0.018 ± 0.012	2.67 ± 0.125	299 ± 12	0.187 ± 0.013
Tz10/54	Sphalérite	Sidi Ahmed	0.414	7.81 ± 0.112	0.103 ± 0.011	19.6 ± 0.750	284 ± 11	0.185 ± 0.013

Table 5. Pb-Pb isotopic ratios of galena.

galènes	$^{206}Pb/^{204}Pb$	± 2σ	$^{207}Pb/^{204}Pb$	± 2σ	$^{208}Pb/^{204}Pb$	± 2σ
Ighrem Aousser vein (3F)						
Tz10.30_1	18,14	0,03	15,54	0,03	37,74	0,09
Tz10.30_4	18,13	0,02	15,54	0,02	37,78	0,06
Tz10.30_5	18,13	0,02	15,54	0,02	37,78	0,07
Tz10.30_6	18,16	0,02	15,56	0,02	37,60	0,05
Tz10.30_7	18,20	0,01	15,62	0,01	37,50	0,03
Sidi Ahmed vein (1270)						
Tz10-31_8	18,23	0,01	15,57	0,01	38,34	0,03
Tz10-31_9	18,26	0,01	15,62	0,01	38,47	0,02
Tz10-31_10	18,27	0,02	15,57	0,03	38,42	0,04
Tz10-35_27	18,50	0,01	15,79	0,01	39,47	0,01
Tz10-35_29	18,40	0,02	15,72	0,02	39,10	0,05
Tz10-35_30	18,43	0,01	15,72	0,01	39,19	0,02
Tz10-35_31	18,38	0,01	15,69	0,01	39,10	0,02
Tz10-35_33	18,41	0,01	15,72	0,01	39,16	0,02
Tz10-35_34	18,47	0,01	15,75	0,01	39,42	0,03
Signal vein(1270)						
Tz10-39_21	18,46	0,010	15,71	0,01	39,30	0,04
Tz10-39_23	18,38	0,016	15,68	0,01	39,08	0,04
Tz10-39_24	18,42	0,019	15,70	0,02	39,11	0,06
Tz11_42Bgal@11	18,127	0,007	15,48	0,01	38,089	0,01
Tz11_42Bgal@12	18,121	0,009	15,48	0,01	38,054	0,02
Tz11_42Bgal@13	18,122	0,007	15,48	0,01	38,089	0,01
Tz11_42Bgal@14	18,152	0,009	15,51	0,01	38,147	0,02
Tz11_42Bgal@15	18,14	0,009	15,51	0,01	38,141	0,02
Tz11_42Bgal@16	18,16	0,007	15,51	0,01	38,182	0,02
Tz11_42Bgal@17	18,14	0,008	15,49	0,01	38,14	0,02
Tz11_42Bgal@18	18,133	0,007	15,50	0,01	38,137	0,02
Tz11_42Bgal@19	18,137	0,007	15,51	0,01	38,15	0,02
Tz11_42Bgal@20	18,127	0,007	15,49	0,01	38,118	0,02
Tz11_42Bgal@21	18,125	0,007	15,49	0,01	38,104	0,02
Tz11_42Bgal@22	18,113	0,007	15,48	0,01	38,094	0,01
Tz11_42Bgal@23	18,127	0,006	15,49	0,01	38,114	0,01
Tz11_42Bgal@24	18,142	0,007	15,50	0,01	38,158	0,01
Tz11_42Bgal@25	18,125	0,006	15,48	0,01	38,081	0,01
Tz11_42Bgal@26	18,129	0,009	15,49	0,01	38,096	0,02
Tz11_42Bgal@27	18,163	0,018	15,55	0,03	38,285	0,10
Tz11_42Bgal@28	18,044	0,015	15,40	0,01	37,746	0,03
Tz11_42Bgal@29	18,082	0,016	15,43	0,01	37,752	0,04
Tz11_42Bgal@30	18,091	0,016	15,43	0,01	37,767	0,03
Tz11_42Bgal@31	18,084	0,011	15,42	0,01	37,73	0,02
Tz11_42Bgal@32	18,081	0,014	15,41	0,01	37,747	0,03
Tz11_42Bgal@33	18,055	0,012	15,40	0,01	37,74	0,02
Tz11_42Bgal@34	18,077	0,013	15,42	0,01	37,768	0,03
Tz11_42Bgal@35	18,06	0,012	15,41	0,01	37,752	0,03

Tz10-43_12	18,23	0,012	15,58	0,01	38,37	0,03
Tz10-43_17	18,39	0,015	15,68	0,01	39,01	0,03
Tz10-43_18	18,40	0,013	15,73	0,01	39,12	0,03
Tz10-43_20	18,44	0,007	15,73	0,01	39,28	0,02

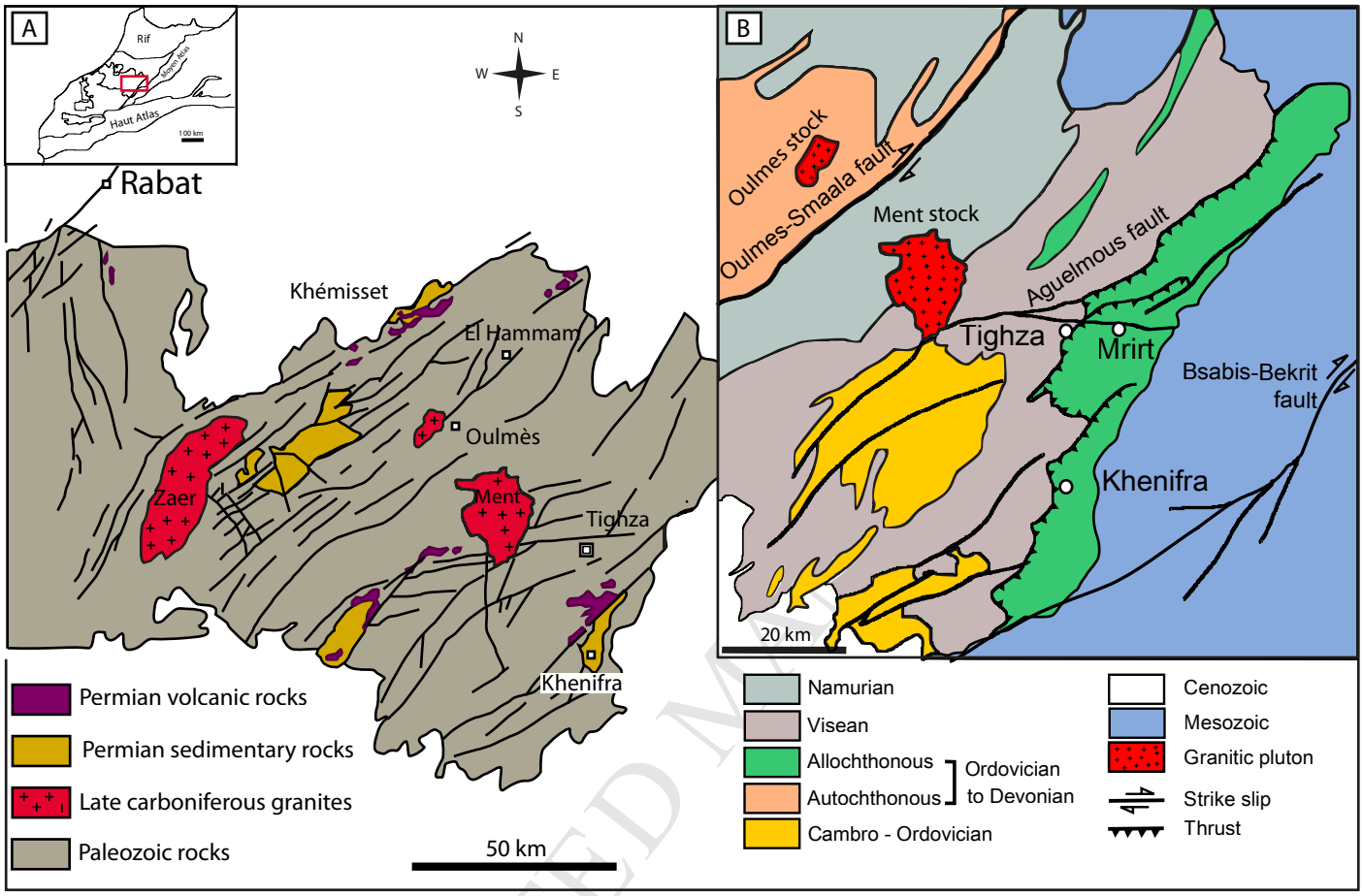

Figure 1 Rossi et al.

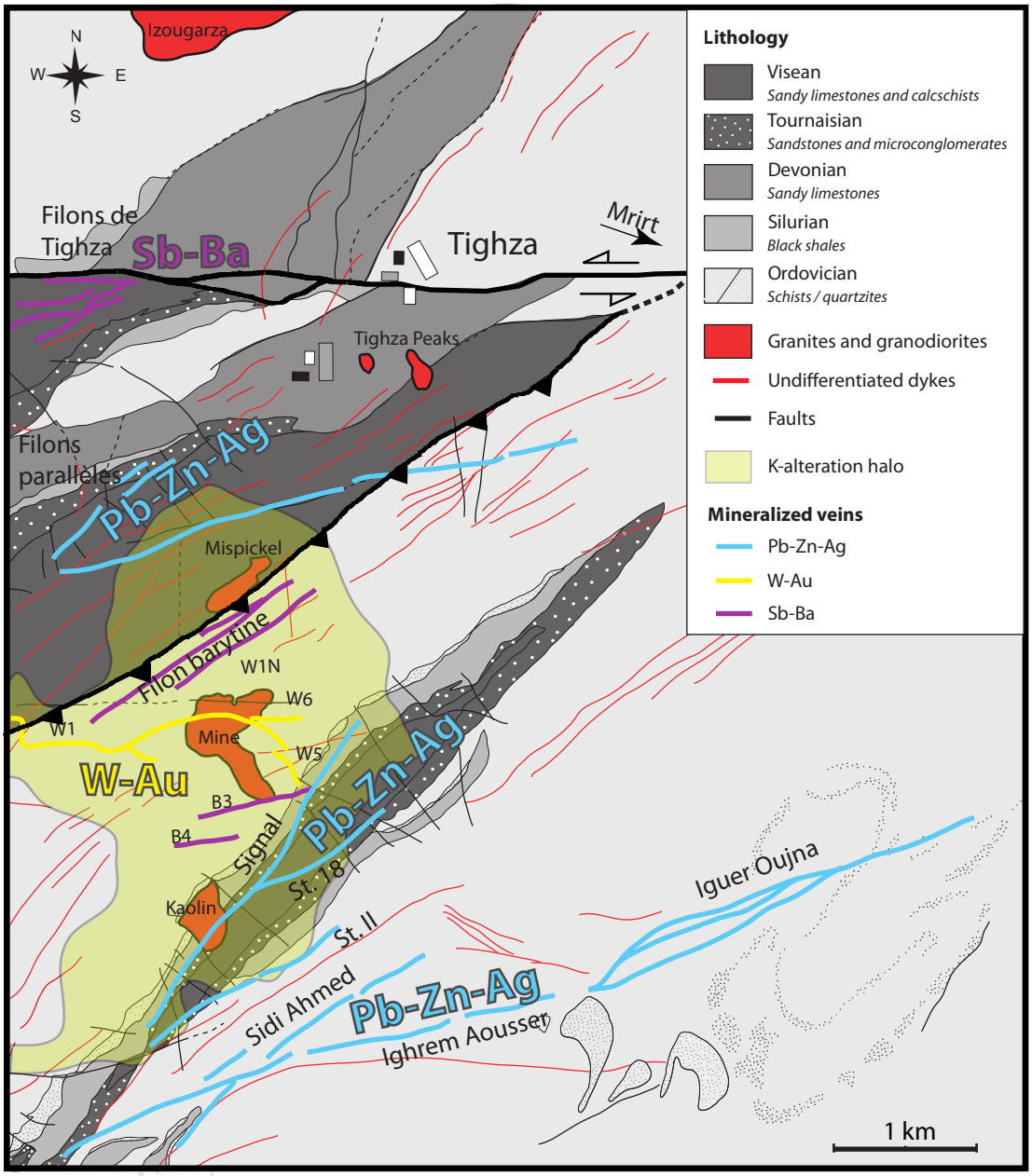

Figure 2 Rossi et al.

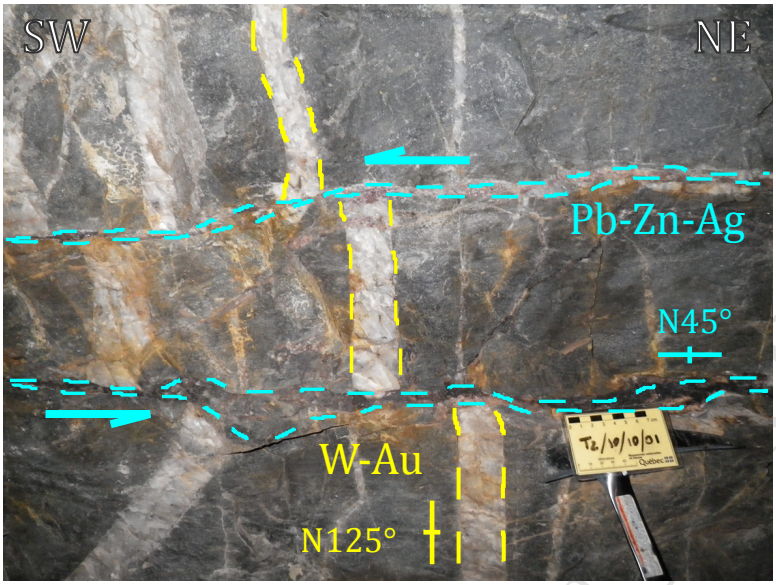

Figure 3 Rossi et al.

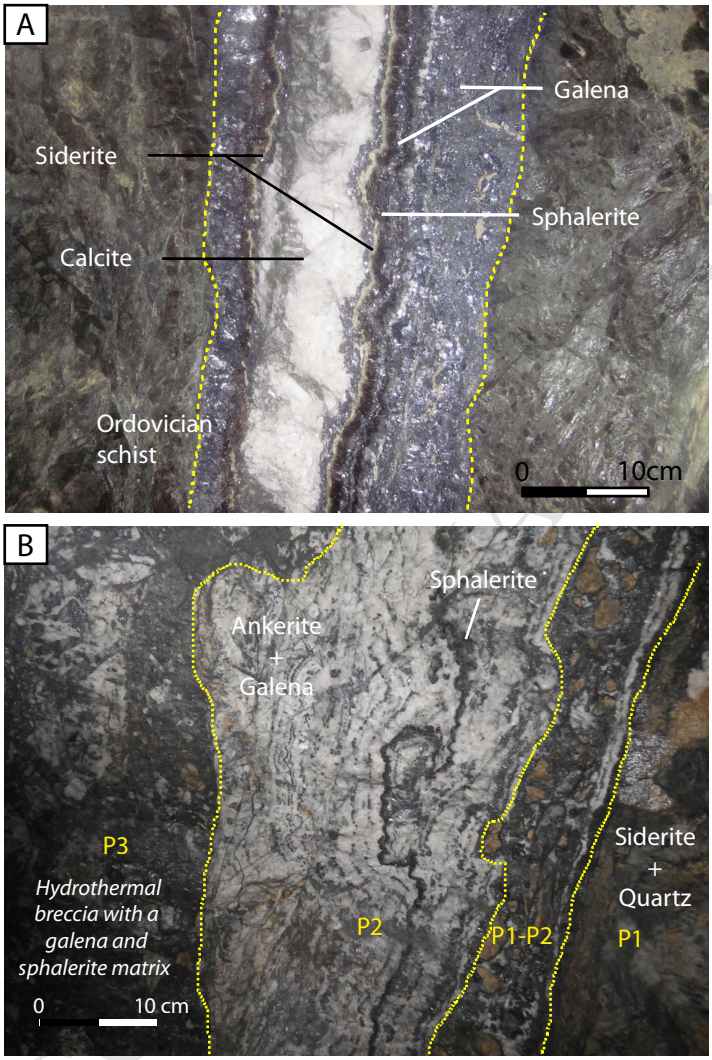

Figure 4

Rossi et al.

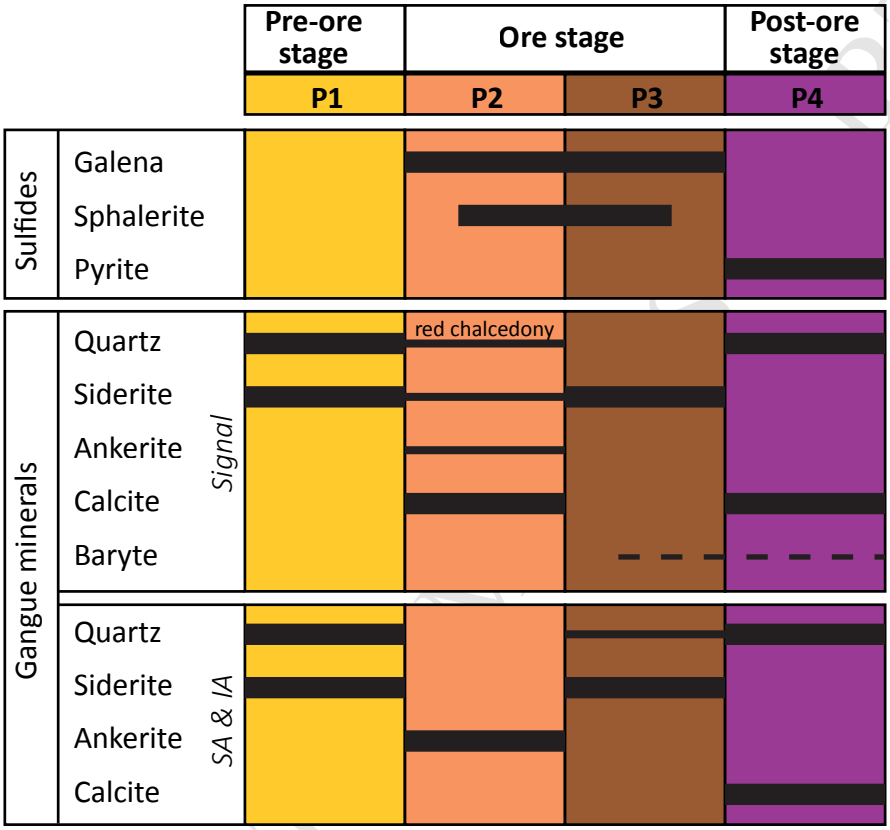

Figure 5

Rossi et al.

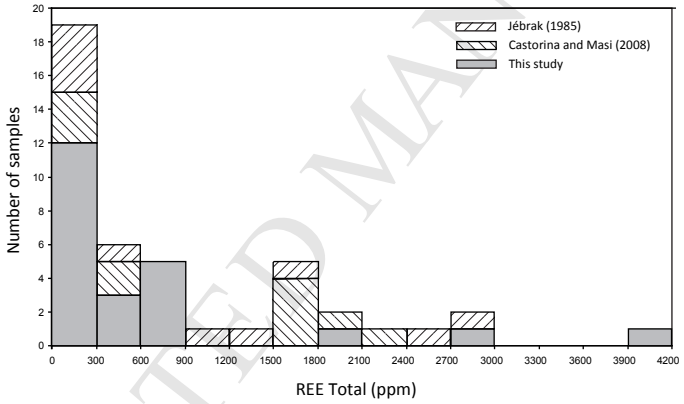

Figure 6 Rossi et al.

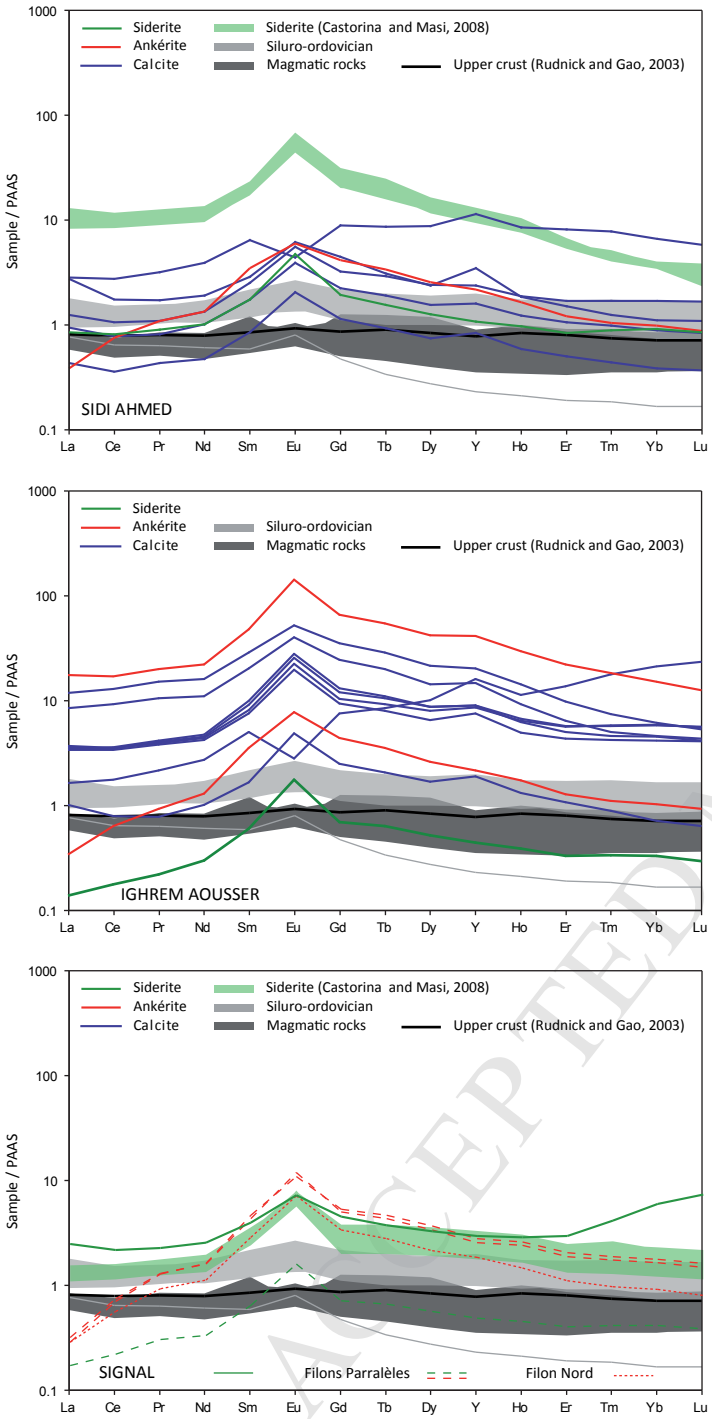

Figure 7

Rossi et al.

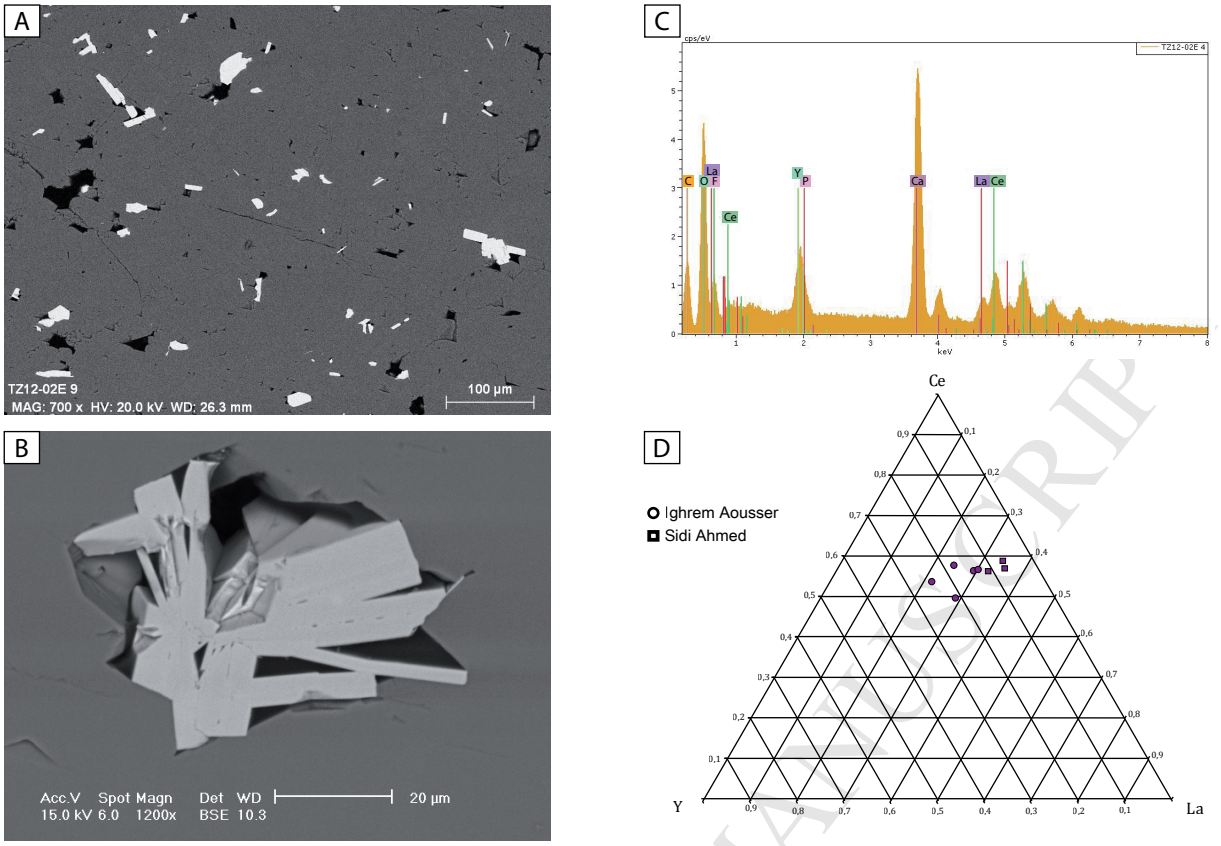

Figure 8

Rossi et al.

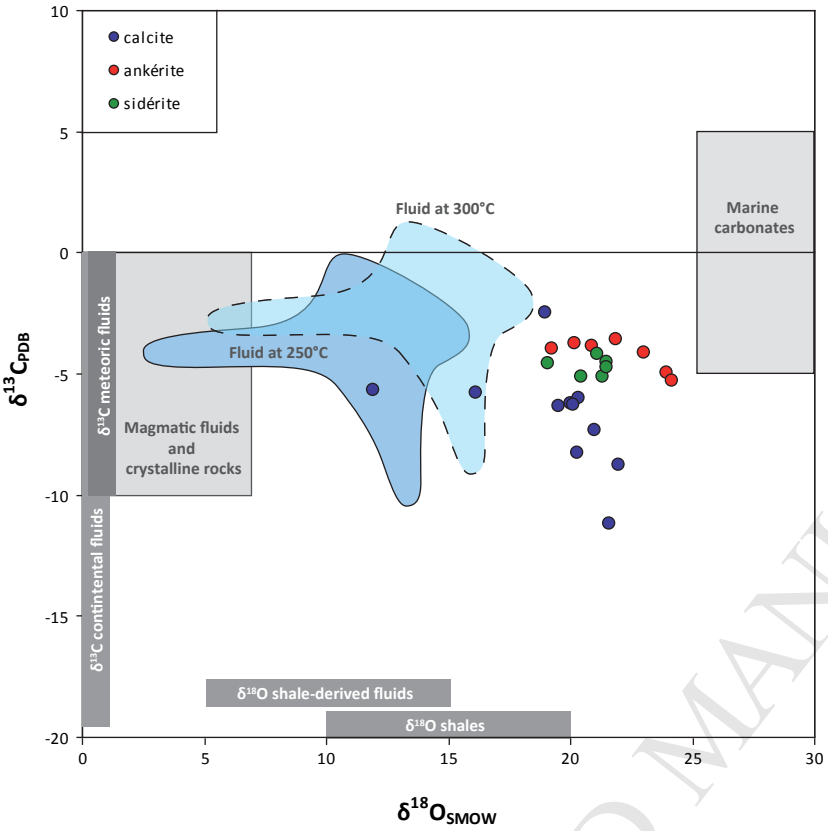

Figure 9

Rossi et al.

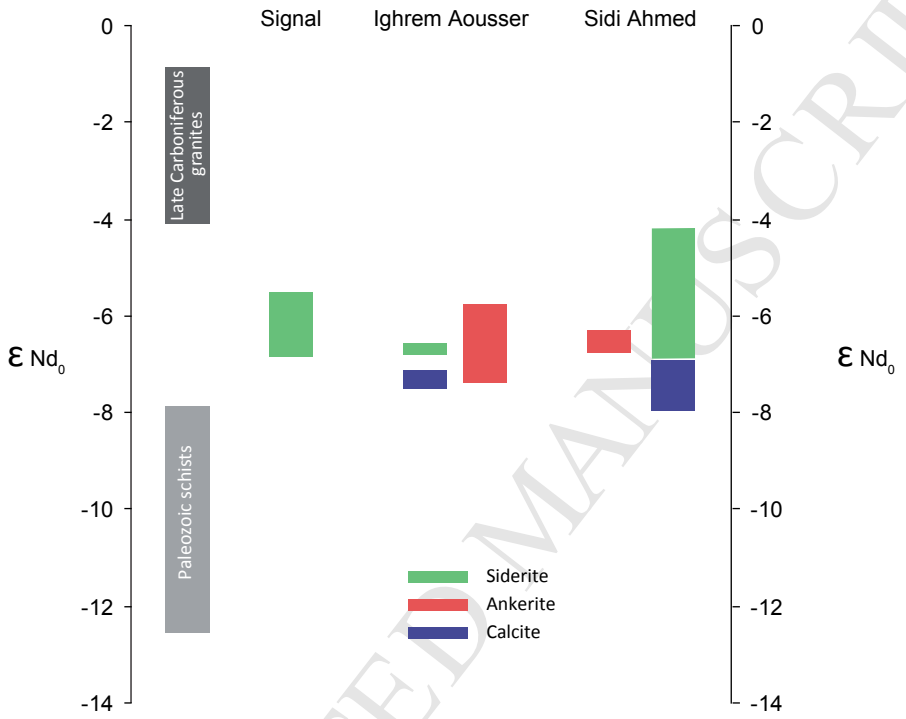

Figure 10

Rossi et al.

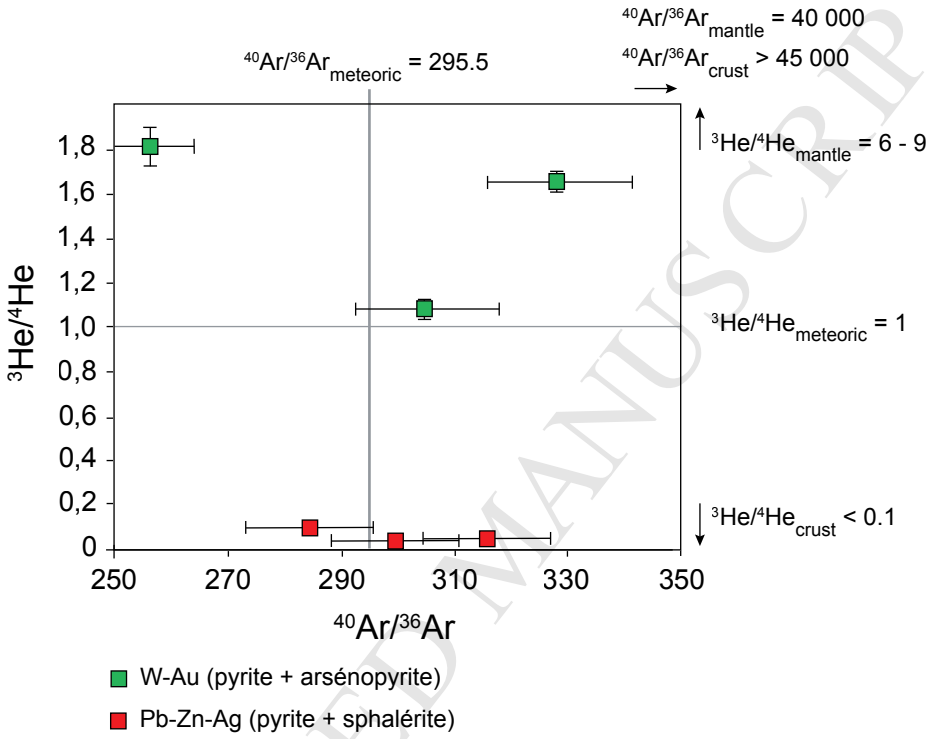

Figure 11 Rossi et al.

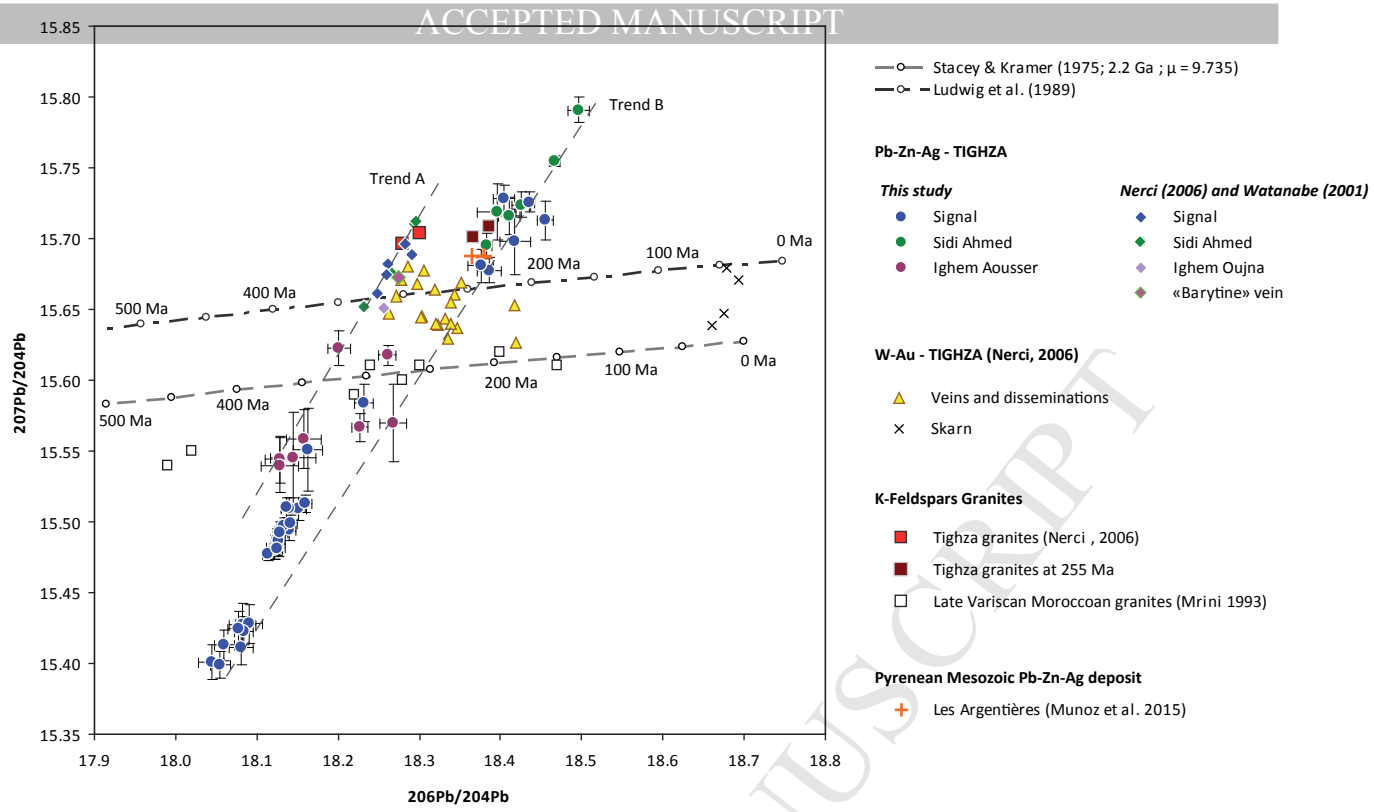

Figure 12 Rossi et al.

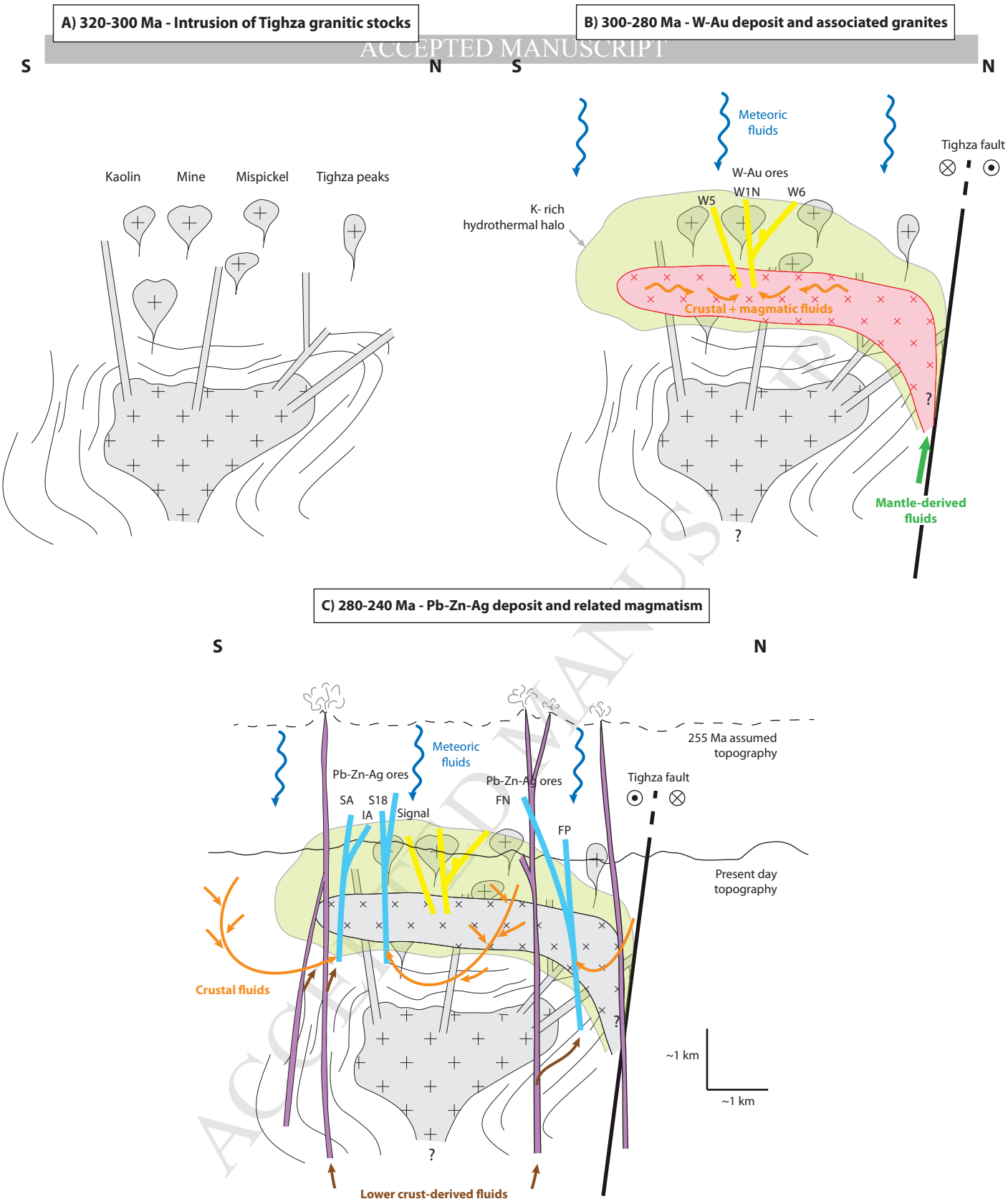

Figure 13

Rossi et al.

Highlights Rossi et al. JAES

- Pb-Zn-Ag vein-type mineralization disconnected from adjacent late-Variscan granites
- Epithermal Pb-Zn-Ag veins related to Permo-Triassic extension and magmatic activity
- Complex hydrothermal system resulting from mixing various crustal fluids
- A new metallogenic model for Pb-Zn-Ag veins and new exploration guides